# 3D analysis of reinforced concrete structural components using a multi-surface elasto-plastic-anisotropic-damage material model

A. Torabizadeh [a], A. Sarikaya [b], R.E. Erkmen [a,*]

[a] *Concordia University, Civil Engineering, Montreal QC H3G 1M8, Canada*
[b] *University of Technology, Sydney NSW 2007, Australia*

## ARTICLE INFO

## ABSTRACT

Elastic-Plastic-Damage material models are widely adopted for the numerical modelling of concrete because of their capability of representing pressure sensitive 3D material behaviour considering permanent inelastic deformations as well as degradation of material moduli beyond the elastic range. In this paper, we develop a non-associative multi-surface plastic-damage material model for the 3D solid element based finite element analysis of reinforced concrete structural components. For the non-associative plastic flow, a linear potential function is adopted, while Menetrey–Willam and Rankine surfaces are adopted as the yield surfaces in compression and tension regimes, respectively. The degradation in the material stiffness under cyclic loading is incorporated by the damage component of the material model, which is generally anisotropic and assumed to be directly dependent on the evolution of the plastic strains. This assumption leads to a computationally efficient algorithm in terms of circumventing iterations to equate the stresses between the coupled damage and plasticity components of the material model. The rigorous details of the developed return-mapping methodology considering both the Cutting-Plane as well as the Closest-Point-Projection algorithms are provided. The material model is employed for the structural level analysis, in which case the concrete bulk is modelled by using an Eight-Node, Six-Degrees-Of-Freedom per-node solid element, and the reinforcement bars and stirrups are modelled by using the conventional Two-Node, Six-Degrees-Of-Freedom per-node Euler–Bernoulli beam-bar element. The inelastic behaviour of the reinforcements is determined by using a simpler elasto-plastic-damage based material model under the assumption of uni-axial stress-strain relations. An in-house fortran software is developed for the computer implementation. Comparisons with results from literature are shown for validation purposes. The validation cases include static analyses of a beam and a column under monotonic loading as well as a shear-wall under cyclic loading.

## 1. Introduction and literature review

In the phenomenological modelling of materials, inelastic behaviour is attributed to two distinct mechanical processes, namely; plasticity (i.e. dislocations along slip planes) and damage (i.e. nucleation and coalescence of cracks). Coupled elasto-plastic-damage theory based phenomenological models have the capability of representing both the permanent deformations due to plastic component and the degradation of elastic moduli due to damage component. Therefore, elasto-plastic-damage models have been widely adopted for the simulation of concrete structural components. In particular for the concrete material, several failure criteria

---

have been proposed by researchers including [1–4]. On the other hand, plasticity theory based simulation of the concrete behaviour requires non-associative flow rule due to the significance of dilatation effects and pressure sensitive material response. Therefore, a potential function generally different from the yield surface is often required to more accurately determine the volumetric component of the plastic flow. Studies that developed non-associative plasticity models based on pressure sensitive yield criteria for the compressive behaviour of concrete include [5–8].

On the other hand, to capture the reduction in stiffness under cyclic loading a damage component is required within the phenomenological material model. To incorporate damage into the behaviour, in [9] the constitutive equations were constructed by partitioning the total strain into the elastic, plastic and damage strain components. Later, several researchers followed this approach including [10] who proposed a methodology to decompose the inelastic strains into plastic and damage components where their contribution to the total inelastic strain was pre-determined based on experimental calibrations. [11] simulated the inelastic behaviour of concrete under cyclic loading in both tension and compression. [12] used a coupled plasticity-damage model for the simulation of the fracture process of plain concrete. [13] developed an elastoplastic-damage model to capture the behaviour of metals considering finite strains and anisotropic damage development. Later, [14] improved the model to capture the behaviour of concrete in both tension and compression. Other coupled plasticity and damage models include the works of [15,16,16–18].

One of the main distinctions between the alternative elastoplastic-damage models in the literature is the way the strain tensor is decomposed. [19] introduced a novel framework for coupled elasto-plastic-damage phenomenological modelling in which the sharing of the total strain was determined based on equilibrium conditions between the updated stresses of the plastic and damage components of the model. The damage evolution problem is posed in a similar form to evolution of plasticity, such that given the damage strain, flow rule and Kuhn–Tucker conditions are applied to determine the damage evolution and stress update within the damage component. The damage strain component is reversible in parallel to the elastic strain, however, the damage evolution is irreversible which is represented by a separate damage variable. Ibrahimbegovic e.g., [20] and his co-workers adopted the framework proposed in [19]. This approach was employed for different material types, including mild steel in [21] and concrete in [22]. Later, [23] identified the necessary predefined relations for the decomposition of the inelastic strains to be able to obtain the widely adopted direct and simple coupling approach introduced for the analysis of concrete material in [11] as a special case within the general elasto-plastic-damage coupling framework of [19]. In [11,23] a single failure surface, potential function and hardening/softening criterion were adopted in order to characterize the inelastic behaviour of concrete, however, the formulations are limited to isotropic damage. In isotropic damage models, the material stiffness matrix is degraded by a scalar damage parameter. However, to simulate direction dependent stiffness degradation effect, anisotropic damage model should be adopted. Several studies adopted symmetric second order damage tensor to consider the damage variations in different directions in the material, which includes the works of [12,24–28]. Damage tensors higher than second order were also developed by [29–31], and [32]. Use of second order damage tensors for anisotropic damage evolution were discussed in detail in [33] and [34]. In this work, we extend the algorithmically efficient elastoplastic damage model introduced in [23] to include anisotropic damage behaviour. Proposed extension to anisotropic damage requires the damage tensor to be built consistent with the plastic return algorithm so that efficiency in circumventing iterations between the damage and plastic evolution can be maintained.

For a full structural level analysis, the tensile behaviour of the concrete material needs to be accurately represented by the material model. The experimental and theoretical works on the concrete plasticity and failure criteria often treats the compressive and tensile behaviour separately due to their different phenomenological characteristics. Studies on the development of the failure criteria for concrete often prioritize the compressive behaviour considering the relative insignificance of the tensile behaviour in reinforced concrete structural capacity. Therefore, to control the tensile behaviour, rather simpler tension cut-off strategy based on Rankine's maximum tensile stress is often deemed sufficient e.g., [35]. As the carefully selected compressive yield surface of concrete grows and shrinks under the hardening and softening law a tensile cut-off is a way to avoid unrealistic tensile strength due to the growth of the compressive surface. Such multi-surface plasticity based modelling approaches for concrete material have been developed by many researchers including [8,36–39]. Elasto-plastic damage based material modelling of concrete with multi-surface yield criteria have been successfully adopted to 3D structural level analysis by several researchers including [40–42]. Introduction of multiple yield surfaces into the material model requires special return mapping algorithms. For geo-materials and concrete in particular, multi-surface return mapping methodologies that involve cut-off surfaces have been developed in [43–47], and [48].

In this paper, we develop a new multi-surface plasticity return mapping procedure for the 3D analysis of reinforced concrete structural components. For the concrete material modelling, we employ the compressive yield surface of [4] with the hardening law developed in [6]. We adopt the Rankine surface for tensile cut-off and the direct elasto-plastic-damage coupling methodology developed by the senior authors in [23]. We also extend the methodology to include anisotropic damage evolution. The methodology is implemented by developing an in-house Fortran program. We present validation case studies by comparing the obtained results with those from the literature.

The outline of this paper is as follows: In Section 2, we review the non-associative multi-surface elasto-plastic-damage material model and set forth the equations. The development of the anisotropic damage compliance is also provided in detail under Section 2. In Section 3, the numerical integration and the return mapping algorithm is presented for the developed non-associative multi-surface elasto-plastic-anisotropic-damage material model. Section 4 is allocated for the specifics of the concrete and steel materials used in the modelling of structural components according to the developed methodology. In Section 5, we describe the solution procedure for the global non-linear equilibrium equations and introduce the finite element types used for the structural level analysis. In Section 6, we present the case studies. We conclude in Section 7.

## 2. Multi-surface elasto-plastic-damage model

### 2.1. Indicial notation of tensor operations

Under this section tensor notations are used and when deemed necessary tensor-orders are also mentioned. We follow the usual convention for the tensorial product operations between second- third- and fourth-order tensors. For clarification, we start by presenting the indicial notation that will be used in future tensor operations under this section. For example, between two second-order tensors when expressed in indicial notation the tensorial product, i.e., $\mathbf{C} = \mathbf{r} \otimes \mathbf{s}$ is a fourth-order tensor which can be written as $C_{ijkl} = r_{ij}s_{kl}$ and double dot product, i.e., $m = \mathbf{r}:\mathbf{s}$ is a scalar, i.e. $m = r_{ij}s_{ij}$. Between two fourth-order tensors the double dot product (or tensorial inner product), i.e., $\mathbf{C} = \mathbf{J}:\mathbf{H}$ is a fourth order tensor, i.e. $C_{ijkl} = J_{ijmn}H_{mnkl}$ or $\mathbf{B} = \mathbf{J} : \mathbf{H}^{\mathbf{T}}$ is $B_{ijkl} = J_{ijmn}H_{klmn}$ or $\mathbf{Z} = \mathbf{J}^{\mathbf{T}}:\mathbf{H}$ is $Z_{ijkl} = J_{mnij}H_{mnkl}$. Between a fourth-order and a second-order tensor the double dot product, i.e. $\mathbf{s} = \mathbf{H}:\mathbf{r}$ is a second-order tensor $s_{ij} = H_{ijkl}r_{kl}$. Between a first-order and second-order tensors when expressed in indicial notation the tensorial product, i.e., $\mathbf{V} = \hat{\mathbf{a}} \otimes \mathbf{s}$ is a third-order tensor which can be written as $V_{ijk} = a_i s_{jk}$. Between a third-order and a second-order tensor the double dot product, i.e. $\hat{\mathbf{b}} = \mathbf{V}:\mathbf{r}$ is a first-order tensor $b_i = V_{ijk}r_{jk}$. Multiplication with a scalar $m$, i.e., $\mathbf{s} = m\mathbf{r}$ can be denoted by using indicial notation as $s_{ij} = mr_{ij}$.

### 2.2. Non-associative multi-surface plasticity

For materials that manifest different strengths under tensile and compressive loads, it is a convenient approach to utilize separate yield surfaces to characterize the stress–strain relation for different loading regime. An advantage of such multi-surface plasticity or composite material models is that they are easier to constitute and calibrate as compared to a single, complicated yield surface. Therefore, composite yield surfaces have been frequently utilized in the modelling of a large variety of geomaterials including soil, rock and concrete. Following the elasto-plastic-damage framework of [19], the second-order total strain increment tensor is additively decomposed as

$$d\boldsymbol{\varepsilon} = d\boldsymbol{\varepsilon}_e + d\boldsymbol{\varepsilon}_p + d\boldsymbol{\varepsilon}_d \tag{1}$$

where $\boldsymbol{\varepsilon}$ is the total strain $\boldsymbol{\varepsilon}_e$ is the elastic strain component, $\boldsymbol{\varepsilon}_p$ is the plastic strain component, $\boldsymbol{\varepsilon}_d$ is the damage strain component and $d$ is the total differential operator.

#### 2.2.1. Plastic flow rule

The non-associative approach is adopted to consider the dilation effects and pressure sensitivity of the concrete material. Accordingly, the direction of the plastic flow is determined from the plastic potential function. For multi-surface plasticity the flow rule can be generalized by using multiple plastic function. Accordingly, the rate independent plastic strain increment can be written using the Koiter's rule (see [49]) as

$$d\boldsymbol{\varepsilon}_p = \sum_{i=1}^{M} d\lambda_{p_i} g_{p_i,\sigma} \tag{2}$$

where $g_{p_i}\left(\boldsymbol{\sigma}, \kappa_{p_i}\right)$ is an active potential surface, $d\lambda_{p_i}$ is the corresponding proportionality factor and $M$ is the number of total active potential surfaces. In Eq. (2) the terms having indices with a comma denote partial differentiation, i.e. $g_{p_i,\sigma} = \partial g_{p_i}/\partial \boldsymbol{\sigma}$ is the gradient of the potential function with respect to the stress tensor. Throughout the document, we refer to each of the active yield surfaces as $f_{p_i}\left(\boldsymbol{\sigma}, \kappa_{p_i}\right)$ and for associative flow rule the potential function $g_{p_i}$ is identical to the corresponding yield function $f_{p_i}$. Both the potential and the hardening surfaces are functions of the stress state $\boldsymbol{\sigma}$ and a hardening function $\kappa_{p_i}$ which is a measure of the evolution of plasticity for each active surface. This indicates that we can write the increment in the plastic hardening function $\kappa_{p_i}$ in terms of the plastic proportionality factor as

$$d\kappa_{p_i} = d\lambda_{p_i} c_{p_i} \tag{3}$$

where $c_{p_i}(\boldsymbol{\sigma}, d\lambda_{p_i})$ is the corresponding hardening factor to be calibrated based on physical experiments.

#### 2.2.2. Consistency condition

During the inelastic deformations, the stresses should stay on the yield surface and therefore, the value of the yield surface stays zero. The proportionality factor is always non-negative as plastic unloading cannot occur due to the irreversibility of plastic deformations and zero proportionality factor indicates elastic only deformations. These conditions known as Kuhn–Tucker conditions of plasticity are summarized below.

$$d\lambda_{p_i} \geq 0, \quad f_{p_i} \leq 0, \quad d\lambda_{p_i} f_{p_i} = 0, \quad 0 < i \leq N \tag{4}$$

where $N$ is the number of total surfaces out of which only $M$ surfaces can be plastically active at a time but one of the Kuhn–Tucker conditions always apply. If the first $M$ surfaces are plastically active and the rest are inactive, one can write the following equations for each group, i.e.

$$f_{p_i} = 0, \quad d\lambda_{p_i} > 0, \quad 0 < i \le M$$
$$f_{p_i} < 0, \quad d\lambda_{p_i} = 0, \quad M < i \le N \tag{5}$$

As the yield surface function value stays zero during a plastic process, the increment in the yield function is also zero, i.e. $df_{p_i} = 0$. Considering that the yield surface is a function of the stress state $\sigma$ and the corresponding hardening function $\kappa_{p_i}$, the total increment of each of the active yield surfaces during plastic deformations can be written as

$$df_{p_i} = \frac{\partial f_{p_i}}{\partial \sigma} : d\sigma + \frac{\partial f_{p_i}}{\partial \kappa_{p_i}} d\kappa_{p_i} = 0, \quad 0 < i \le M \tag{6}$$

Note that in Eq. (6) both $\partial f_{p_i}/\partial \sigma$ and $\sigma$ are second order tensors and we indicate tensorial inner product with the symbol (:). Considering that the stress increments can only be elastic, i.e. $d\sigma = \mathbf{E} : d\varepsilon_e$ and using Eqs. (1), (2) and from Eq. (6) one obtains

$$d\sigma = \mathbf{E} : \left( d\varepsilon - \sum_{j=1}^{M} d\lambda_{p_j} \mathbf{g}_{p_j,\sigma} - d\varepsilon_d \right) \tag{7}$$

that satisfies the plastic consistency condition, where $\mathbf{E}$ is the fourth order elasticity tensor. By using Eqs. (3) and (6) in Eq. (7), the consistency condition can be re-written as

$$df_{p_i} = \frac{\partial f_{p_i}}{\partial \sigma} : \mathbf{E} : \left( d\varepsilon - \sum_{j=1}^{M} d\lambda_{p_j} \mathbf{g}_{p_j,\sigma} - d\varepsilon_d \right) + \frac{\partial f_{p_i}}{\partial \kappa_{p_i}} d\lambda_{p_i} c_i = 0, \quad 0 < i \le M \tag{8}$$

which is an equation for each of the $M$ active surfaces from which $M$ proportionality factor $d\lambda_{p_i}$ needs to be determined. Thus, in Eq. (8) the proportionality factors $d\lambda_{p_i}$ are treated as the primary unknowns because the increments in the plastic strain and the hardening function given in Eqs. (2) and (3), respectively can be determined once the proportionality factors are known. As we will see next, we will also be able to determine the damage evolution as a result of the plastic evolution and, the damage strain component in Eq. (1) is treated herein such that it is indeed conveniently calculated once the proportionality factor $d\lambda_{p_i}$ is known. As a result the stresses can be updated from Eq. (7). However, Eq. (8) is a non-linear differential equation which generally requires a numerical procedure to solve for $d\lambda_{p_i}$.

### 2.3. Damage component of the material model

The role of the damage component of the material model is to effectively cause reduction in the elastic material moduli according to the progress of damage. For that purpose, we define the fourth-order damage compliance tensor $\mathbf{D}$ and additively decompose it into isotropic and anisotropic components as

$$\mathbf{D} = \phi \mathbf{E}^{-1} + \mathbf{Y} \tag{9}$$

in which, $\phi$ is the isotropic damage parameter and $\mathbf{Y}$ is the anisotropic damage contribution. Accordingly, the total damage strain can then be obtained as

$$\varepsilon_d = \mathbf{D} : \sigma \tag{10}$$

The effect of damage on the stress tensor can also be cast into the incremental form similar to plasticity, by substituting Eq. (9) into the increment of the damage strain $d\varepsilon_d$ using Eq. (10) and also using the product rule for differentiation in $\mathbf{D} : d\sigma = d(\mathbf{D} : \sigma) - d\mathbf{D} : \sigma$, i.e.

$$d\sigma = \mathbf{D}^{-1} : d\varepsilon_d - \mathbf{D}^{-1} : \sum_{i=1}^{M} d\lambda_{d_i} \mathbf{g}_{d_i,\sigma} \tag{11}$$

where

$$d\mathbf{D} : \sigma = \sum_{i=1}^{M} d\lambda_{d_i} \mathbf{g}_{d_i,\sigma} \tag{12}$$

defines the damage flow that satisfies the damage consistency condition, considering $M$ active damage surfaces, in which $d\lambda_{d_i}$ are the damage proportionality factors, $g_{d_i}\left(\sigma, \kappa_{d_i}\right)$ are the corresponding potential functions and $\kappa_{d_i}$ are the damage hardening functions. One can refer to the framework proposed in [19] for this incremental setting in parallel to plasticity equations and the works of [20] and his co-workers for its implementation. In this setting, the damage evolution is also controlled by a damage surface and in the case of non-associative flow, a separate damage potential surface. According to the damage consistency condition, i.e., $df_{d_i} = 0$, the damage proportionality factors $d\lambda_{d_i}$ are determined similar to plasticity equations. In the following, we adopt a special case of this general framework where a separate group of surfaces are not required.

### 2.3.1. Direct coupling

In our approach, we determine the damage as a result of the evolution of plasticity parameter. To be able to achieve that as a special case of a more general frame-work of [19], we set the following relations

$$f_p\left(\boldsymbol{\sigma}, \kappa_p\right) = f_d\left(\boldsymbol{\sigma}, \kappa_d\right) \tag{13}$$

$$g_p\left(\boldsymbol{\sigma}, \kappa_p\right) = g_d\left(\boldsymbol{\sigma}, \kappa_d\right) \tag{14}$$

$$c_p\left(\boldsymbol{\sigma}, \kappa_p\right) = c_d\left(\boldsymbol{\sigma}, \kappa_d\right) \tag{15}$$

$$d\varepsilon_d = \mathbf{P} : d\varepsilon \tag{16}$$

$$d\lambda_d = \bar{\phi}d\lambda_p \tag{17}$$

$$d\kappa_d = \bar{\phi}d\kappa_p, \tag{18}$$

which is a result of Eqs. (3) and (17). The operator $\mathbf{P}$ in Eq. (16) can be written as

$$\mathbf{P} = \mathbf{D} : \mathbf{M} : \mathbf{E} \tag{19}$$

in which $\mathbf{M} = (\mathbf{I} + \mathbf{E} : \mathbf{D})^{-1}$ (see [19]). The operator $\mathbf{P}$ is adopted herein to determine the damage component of the strain directly from the total strain so that plastic strain update can be processed independent of the damage update, after which the damage evolution follows according to the operator $\mathbf{P}$ which will later be defined as a function of total plastic strains. The scalar $\bar{\phi}$ introduced in Eq. (17) can be written as

$$\bar{\phi} = \frac{\boldsymbol{\varepsilon}_p{}^T : \mathbf{E} : \boldsymbol{\varepsilon}_p}{\boldsymbol{\varepsilon}_p{}^T : \mathbf{D}^{-1} : \boldsymbol{\varepsilon}_p} \tag{20}$$

which is also a function of total plastic strains. Later, we will prove that these conditions provide consistency of evolution between the damage and plasticity components of the material within the frame-work of [19]. This approach is the extension of the method introduced in [23], which was limited to isotropic damage, to anisotropic damage. The motivation behind this approach is the computational efficiency of splitting the plastic return and damage update operations such that after satisfying the plastic consistency conditions no further iterations are required to satisfy the consistency between the plastic and damage update.

### 2.3.2. Consistency between damage strain rate and evolution of plasticity

The stress–strain relationship considering the damage strain can be written as

$$\boldsymbol{\sigma} = \mathbf{E} : \left(\boldsymbol{\varepsilon} - \boldsymbol{\varepsilon}_p - \boldsymbol{\varepsilon}_d\right) \tag{21}$$

The strain equivalence hypothesis (see [50]) states that the strain associated with a damaged state under the applied stress is equivalent to the strain associated with its fictitious undamaged state under effective stress, which is defined as $\bar{\boldsymbol{\sigma}} = \mathbf{M}^{-1} : \boldsymbol{\sigma}$. In-line with the hypothesis of strain equivalence the effective stress is $\bar{\boldsymbol{\sigma}} = \mathbf{E} : (\boldsymbol{\varepsilon} - \boldsymbol{\varepsilon}_p)$, i.e. $\boldsymbol{\sigma} = \mathbf{M} : \mathbf{E} : (\boldsymbol{\varepsilon} - \boldsymbol{\varepsilon}_p)$. By using this relation, the damage strain becomes

$$\boldsymbol{\varepsilon}_d = \mathbf{P} : \left(\boldsymbol{\varepsilon} - \boldsymbol{\varepsilon}_p\right) \tag{22}$$

Using Eqs. (21) and (22), the stress–strain relationship of damaged material, i.e., $\boldsymbol{\sigma} = \mathbf{E} : \left(\boldsymbol{\varepsilon} - \boldsymbol{\varepsilon}_p - \boldsymbol{\varepsilon}_d\right)$ can be exchanged with that of the fictitious undamaged state, i.e.,

$$\boldsymbol{\sigma} = \mathbf{E} : (\mathbf{I} - \mathbf{P}) : \left(\boldsymbol{\varepsilon} - \boldsymbol{\varepsilon}_p\right) \tag{23}$$

It should be noted that the stress as expressed in Eq. (23) is the result of operator splitting, which is the result of the imposed condition in Eq. (16). However, for the total damage strain expression of Eq. (10) to be consistent with the damage strain rate presented in Eq. (16), the last three terms in the total derivative of the damage strain expression should vanish, which can be obtained from Eq. (22), i.e., $d\boldsymbol{\varepsilon}_d = \mathbf{P} : d\boldsymbol{\varepsilon} + d\mathbf{P} : \boldsymbol{\varepsilon} - \mathbf{P} : d\boldsymbol{\varepsilon}_p - d\mathbf{P} : \boldsymbol{\varepsilon}_p$, from which one obtains the relation

$$d\mathbf{P} : \left(\boldsymbol{\varepsilon} - \boldsymbol{\varepsilon}_p\right) = \mathbf{P} : d\boldsymbol{\varepsilon}_p \tag{24}$$

From Eqs. (12) and (17), one obtains

$$d\mathbf{D} : \boldsymbol{\sigma} = \bar{\phi}d\boldsymbol{\varepsilon}_p \tag{25}$$

By using Eqs. (10), (21) and (22), and substituting into Eq. (23), one obtains

$$d\mathbf{D} : \mathbf{E} : (\mathbf{I} - \mathbf{P}) : (\boldsymbol{\varepsilon} - \boldsymbol{\varepsilon}_p) = \bar{\phi}d\boldsymbol{\varepsilon}_p \tag{26}$$

From Eqs. (10), (19), (22) and (23), one obtains

$$\mathbf{E} : (\mathbf{I} - \mathbf{P}) = \mathbf{M} : \mathbf{E} \tag{27}$$

Under the assumption of $d\varepsilon_d = \mathbf{P} : d\varepsilon$, the stress update based on plasticity in Eq. (7) can be written as

$$d\boldsymbol{\sigma} = \mathbf{E} : \left[(\mathbf{I} - \mathbf{P})d\varepsilon - d\varepsilon_p\right] \tag{28}$$

On the other hand, under the assumption of $d\varepsilon_d = \mathbf{P} : d\varepsilon$ the stress update based on plasticity in Eq. (11) can be alternatively written as

$$d\boldsymbol{\sigma} = \mathbf{D}^{-1} : \mathbf{P} : d\varepsilon - \bar{\phi}\mathbf{D}^{-1} : d\varepsilon_p \tag{29}$$

The condition of agreement between the two alternative stress rates in Eqs. (28) and (29) can be found by using Eq. (27) in Eq. (28) and then using Eq. (19) in Eq. (29) which reduces to

$$\mathbf{D} : \mathbf{E} : d\varepsilon_p = \bar{\phi}d\varepsilon_p \tag{30}$$

### 2.3.3. Anisotropic damage component

For the purpose of computational efficiency, we adopt Eq. (30) for the total plastic strain and develop an anisotropic damage compliance $\mathbf{D}$ based on the relationship

$$\mathbf{D} : \mathbf{E} : \varepsilon_p = \bar{\phi}\varepsilon_p \tag{31}$$

in which plastic strain $\varepsilon_p$ is the eigenvector and $\bar{\phi}$ is the eigenvalue. Based on Eq. (31), the compliance matrix is directly related to the accumulated plastic deformations. To satisfy the above relation at any stage of loading, we formulate the anisotropic part of the damage compliance, i.e. $\mathbf{Y}$ as

$$\mathbf{Y} = \omega\varepsilon_p \otimes \varepsilon_p : \mathbf{E}^{-1} \tag{32}$$

in which $\omega$ is designated as a calibration scalar. On the other hand, the isotropic component of the damage compliance identically satisfies Eq. (31). Thus, by substituting Eq. (32), into Eq. (9), it can be shown that Eq. (31) is always satisfied.

### 2.3.4. Isotropic damage component

For isotropic only damage it can be verified that $\bar{\phi} = \phi$, and

$$\mathbf{D} : \mathbf{E} = \phi\mathbf{I} \tag{33}$$

In [23], Eq. (33) was proven to be a special case of Eq. (22), and the damage strain was conveniently described in terms of the total and plastic strains as

$$\varepsilon_d = \varphi\varepsilon - \varphi\varepsilon_p \tag{34}$$

Note that for only isotropic damage, the effective stress, i.e. $\boldsymbol{\sigma}/(1 - \varphi)$ considering the load carrying area is reduced by the factor of $(1 - \varphi)$ and Eq. (23) becomes

$$\boldsymbol{\sigma} = (1 - \varphi)\mathbf{E} : \left(\varepsilon - \varepsilon_p\right) \tag{35}$$

For isotropic damage, the equivalence of Eq. (35) to Eq. (21) under the hypothesis of strain equivalence and conditions set in Eqs. (13) to (34) was proven in [23]. Many authors e.g. [11,17] preferred the relationship in Eq. (35) instead of (21), where the development of damage can also be defined directly as a function of the plastic evolution in the form of

$$\varphi = \varphi(\kappa_{p_i}), \quad 0 < i \leq M \tag{36}$$

Following the conventional meaning of the isotropic damage parameter $\phi$ introduced in Eq. (9), we relate it to the measure of reduction in the load carrying area, i.e. $\varphi$ as $\phi = \varphi/(1 - \varphi)$, where $\varphi \in [0, 1]$.

Next, we provide the detailed numerical procedure for the stress update, in which the anisotropic damage compliance is also introduced in matrix form under Section 3.4. Further specifics of the plasticity dependent damage evolution functions for the concrete and steel materials will be presented later under Section 4.

## 3. Computational algorithm for the material model

For the numerical algorithm, we cast the equations in finite incremental form

$$\boldsymbol{\sigma}_{(n)} = \mathbf{E}(\mathbf{I} - \mathbf{P}_{(n)})(\varepsilon_{(n)} - \varepsilon_{p_{(n)}}) \tag{37}$$

where we use the subscript $(n)$ to refer to the last converged step of the material level stress return algorithm. Thus, $\boldsymbol{\sigma}_{(n)}$ is the last converged stress. It should be noted that algorithm related indices are written in parenthesis. We use sub-scripts for the step and superscripts for iterations within the step. Within the next step after convergence, i.e., in the current step of interest $(n + 1)$, we

collect the strain $\boldsymbol{\varepsilon}_{(n+1)}$ from the global algorithm and initially we assume the strain increment $\Delta\boldsymbol{\varepsilon}_{(n+1)} = \boldsymbol{\varepsilon}_{(n+1)} - \boldsymbol{\varepsilon}_{(n)}$ is fully elastic. Thus, we define the trial stress assuming a full elastic increment, i.e.

$$\boldsymbol{\sigma}_{(n+1)}^{\text{trial}} = \boldsymbol{\sigma}_{(n)} + \mathbf{E}\Delta\boldsymbol{\varepsilon}_{(n+1)} \tag{38}$$

Note that for the numerical calculations, we drop the tensor notation and treat the stress, strain and elastic tensors as vectors and matrices by adopting the Voigt notation. If the trial stress in Eq. (38) is elastic within the yield surface limits (which might be due to unloading or re-loading), then we make a correction to the final stress considering the existing damage state as

$$\boldsymbol{\sigma}_{(n+1)} = \boldsymbol{\sigma}_{(n)} + \mathbf{E}(\mathbf{I} - \mathbf{P}_{(n)})\Delta\boldsymbol{\varepsilon}_{(n+1)} \tag{39}$$

where $\mathbf{P}_{(n+1)} = \mathbf{P}_{(n)}$ due to the fact that no plastic deformations occurred during the last step. If the trial stress calculated in Eq. (38) is within the elastic limit, then we assume that the updated stress in Eq. (39) is also within the elastic limit. This procedure assures complete independence of the plastic return operations from the damage update.

On the other hand, if the trial stress state exceeds the elastic limit the plastic return mapping algorithm is activated and the stress is updated as

$$\boldsymbol{\sigma}_{(n+1)} = \boldsymbol{\sigma}_{(n)} + \mathbf{E}(\Delta\boldsymbol{\varepsilon}_{(n+1)} - \Delta\boldsymbol{\varepsilon}_{p_{(n+1)}}) \tag{40}$$

where $\boldsymbol{\sigma}_{(n+1)}$ is the stress after convergence of the plastic return mapping at the end of the current step $(n+1)$. In Eq. (40), $\Delta\boldsymbol{\varepsilon}_{p_{(n+1)}}$ is the total plastic strain accumulated within step $(n+1)$, which often requires iterative calculations, i.e.

$$\Delta\boldsymbol{\varepsilon}_{p_{(n+1)}}^{(k)} = \Delta\boldsymbol{\varepsilon}_{p_{(n+1)}}^{(k-1)} + \delta\boldsymbol{\varepsilon}_{p_{(n+1)}}^{(k)} \tag{41}$$

where the symbol $\delta$ indicates increment within each iteration $(k)$ referred with a superscript, which should be contrasted with the use of the symbol $\Delta$ which refers to the total increment within the step $(n+1)$. Thus, after final iteration leading to convergent mapping, the updated strain in Eq. (41) produces $\Delta\boldsymbol{\varepsilon}_{p_{(n+1)}} = \Delta\boldsymbol{\varepsilon}_{p_{(n+1)}}^{(k_{final})}$. So, the problem at hand is to find the plastic strain increment, i.e. $\delta\boldsymbol{\varepsilon}_{p_{(n+1)}}^{(k)}$ in each iteration $(k)$ of the current step $(n+1)$, which is explained next.

### 3.1. Determination of plastic deformations

To find the plastic strain change in each iteration, we first refer to the incremental–iterative form of Eq. (2), i.e.

$$\delta\boldsymbol{\varepsilon}_{p_{(n+1)}}^{(k)} = \sum_{j=1}^{N} \delta\lambda_{p_j}^{(k)} \mathbf{g}_{p_j,\boldsymbol{\sigma}}^{(k)} \tag{42}$$

Note the sub-script $(n+1)$ is dropped on the right hand side of Eq. (42) for simplicity in notations. However, it should be trivial that the iterations are taking place always within the current step $(n+1)$. In Eq. (42), both the proportionality factor and the gradient of the potential function carry the superscript $(k)$ to indicate that their values are updated in each iteration. The iterative proportionality factor is indeed the primary unknown which is to be extracted from the iterative incremental form of Eq. (8), which can be written as

$$\delta\mathbf{f}^{(k)} = \delta\mathbf{b}^{(k)} - \mathbf{A}^{(k)}\delta\boldsymbol{\lambda}^{(k)} \tag{43}$$

in which $\delta\mathbf{f}^{(k)}$ is a zero vector as a result of the consistency condition. From Eq. (43), the proportionality factor $\delta\boldsymbol{\lambda}^{(k)}$ can be solved as

$$\delta\boldsymbol{\lambda}^{(k)} = \mathbf{A}^{(k)^{-1}}\delta\mathbf{b}^{(k)} \tag{44}$$

At this point, to write the components in Eq. (44) explicitly, we bring the assumption that the total number of active surfaces can at most be two. Later in Section 4, we specify our multi-surface plasticity model for the concrete with only two surfaces, i.e. $N=2$. For a general two-surface plasticity model, the matrix $\mathbf{A}^{(k)}$ in Eq. (43) can be explicitly written as

$$\mathbf{A}^{(k)} = \begin{bmatrix} a_{11}^{(k)} & a_{12}^{(k)} \\ a_{21}^{(k)} & a_{22}^{(k)} \end{bmatrix} = \begin{bmatrix} \mathbf{n}_1^{(k)\text{T}}\mathbf{R}^{(k)}\mathbf{m}_1^{(k)} + f_{p_1,\kappa_1}^k c_1^{(k)} & \mathbf{n}_1^{(k)\text{T}}\mathbf{R}^{(k)}\mathbf{m}_2^{(k)} \\ \mathbf{n}_2^{(k)\text{T}}\mathbf{R}^{(k)}\mathbf{m}_1^{(k)} & \mathbf{n}_2^{(k)\text{T}}\mathbf{R}^{(k)}\mathbf{m}_2^{(k)} + f_{p_2,\kappa_2}^{(k)} c_2^{(k)} \end{bmatrix} \tag{45}$$

in which

$$\mathbf{m}_i^{(k)} = \mathbf{g}_{p_i,\boldsymbol{\sigma}}^{(k)}, \quad 0 < i \le 2 \tag{46}$$

$$\mathbf{n}_i^{(k)} = \mathbf{f}_{p_i,\boldsymbol{\sigma}}^{(k)}, \quad 0 < i \le 2 \tag{47}$$

$$\mathbf{R}^{(k)} = \left(\mathbf{E}^{-1}\mathbf{Q}^{(k)}\right)^{-1} \tag{48}$$

were defined. We note that in deriving Eq. (45) the hardening functions are assumed uncoupled. In Eq. (48), the matrix $\mathbf{Q}_i$ is defined as

$$\mathbf{Q}^{(k)} = \left(\mathbf{I} + \mathbf{E}\sum_{j=1}^{N=2} \Delta\lambda_{p_j}^{(k)}\mathbf{H}_j^{(k)}\right) \tag{49}$$

in which $\mathbf{I}$ is the identity matrix and $\mathbf{H}_i$ is the Hessian matrix of the active potential surface, i.e.

$$\mathbf{H}_i^{(k)} = \mathbf{m}_{i,\sigma}^{(k)}, \quad 0 < i \leq 2 \tag{50}$$

On the other hand, the vector $\delta\mathbf{b}^{(k)}$ in Eq. (43) can be written as

$$\delta\mathbf{b}^{(k)} = \mathbf{f}^{(k)} - \mathbf{h}^{(k)} \tag{51}$$

in which $\mathbf{f} = \left\langle f_{p_1} \; f_{p_2} \right\rangle^{\mathrm{T}}$ and the superscript $(k)$ indicates that the yield surface values used in Eq. (51) are updated in each iteration, i.e.

$$f_{p_i}^{(k)} = f_{p_i}(\sigma_{(n+1)}^{(k)}, \kappa_{p_i}^{(k)}), \quad 0 < i \leq 2 \tag{52}$$

where

$$\sigma_{(n+1)}^{(k)} = \sigma_{(n)} + \mathbf{E}(\Delta\varepsilon_{(n+1)} - \Delta\varepsilon_{p_{(n+1)}}^{(k)}) \tag{53}$$

and

$$\kappa_{p_i}^{(k)} = \kappa_{p_i}^{(k-1)} + \delta\kappa_{p_i}^{(k)}, \quad 0 < i \leq 2 \tag{54}$$

In Eq. (51) the vector $\mathbf{h}^{(k)}$ is defined as

$$\mathbf{h}^{(k)} = \left\{ \begin{matrix} h_1^{(k)} \\ h_2^{(k)} \end{matrix} \right\} \tag{55}$$

whose components can be written as

$$h_i^{(k)} = \mathbf{n}_i^{(k)\mathrm{T}} \mathbf{R}_i^{(k)} \mathbf{E}^{-1} \mathbf{r}_i^{(k)}, \quad 0 < i \leq 2 \tag{56}$$

To derive vector $\delta\mathbf{b}^{(k)}$ in Eq. (43) in finite incremental form, we replace the consistency condition, $d\mathbf{b} = f_{,\sigma} : \mathbf{E} : d\varepsilon$ with the finite incremental form of the consistency condition. For this purpose, first we refer to the finite form of the yield condition i.e.

$$f_{p_i}^{(k)} = 0 \tag{57}$$

which is then truncated using first order Taylor series approximation in the neighbour of the trial stress $\sigma_{(n+1)}^{\mathrm{trial}}$. From Eq. (40), the converged stress state that satisfies the consistency condition can be written in terms of the trial stress as

$$\sigma_{(n+1)} = \sigma_{(n+1)}^{\mathrm{trial}} - \mathbf{E}\Delta\varepsilon_{p_{(n+1)}} \tag{58}$$

Backward-Euler finite difference procedures derived from the first order Taylor series expansion are commonly adopted as time-stepping procedures, e.g., in [43], which in our context lead to Eq. (43). Furthermore, two of the most commonly adopted time stepping procedures for plasticity are Closest Point Projection and Cutting Plane Algorithms. Both are Elastic-Prediction-Plastic-Correction procedures in which, when triggered the return mapping to yield surface is performed after a full elastic assumption, for which the second term on the right of Eq. (58) is pursued. Thus, plastic strain is assumed zero for the initial iteration, i.e. $\delta\varepsilon_{p_{(n+1)}}^{(0)} = \mathbf{0}$. On the other hand, the stress state in the gradients of the potential and yield surfaces in Eqs. (46) and (47), respectively determine whether the algorithm is Cutting Plane or Closest Point Projection. For calculating the gradients, while the former algorithm uses the stress state at the end of the previous iteration, i.e. $\sigma_{(n+1)}^{(k-1)}$, the later uses the updated stress state, i.e. $\sigma_{(n+1)}^{(k)}$. To implement the Cutting Plane Algorithm, one enforces the satisfaction of the yield condition in iterations i.e., $f_{p_i}^{(k)} < tol$. In addition, the Closest Point Projection Algorithm employs the first order Taylor approximation of the finite form of the flow rule so that the direction between the trial and the converged stress is enforced to be the closest-point projection direction from the trial stress point $\sigma_{(n+1)}^{\mathrm{trial}}$ towards the last updated stress $\sigma_{(n+1)}^{(k)}$, i.e.

$$\mathbf{r}^{(k)} = \sigma_{(n+1)}^{(k)} - \sigma_{(n+1)}^{\mathrm{trial}} + \mathbf{E} \sum_{j=1}^{N=2} \Delta\lambda_{p_j}^{(k)} \mathbf{m}_j^{(k)} \tag{59}$$

where $\mathbf{r}^{(k)}$ is a residual vector that should also vanish at the end of the iterations, i.e. $\| \sum_{j=1}^{N=2} \Delta\lambda_{p_j}^{(k)} \mathbf{m}_j^{(k)} - \Delta\varepsilon_{p_{(n+1)}}^{(k)} \| < tol$. The proportionality factor components in Eqs. (49) and (59) are updated as

$$\Delta\lambda_{p_i}^{(k)} = \Delta\lambda_{p_i}^{(k-1)} + \delta\lambda_{p_i}^{(k)}, \quad 0 < i \leq 2 \tag{60}$$

To find a solution that satisfies both conditions $f_{p_i}^{(k)} = 0$ and $\|\mathbf{r}^{(k)}\| = 0$ of Closest Point Projection Algorithm, one can implement the Newton–Raphson solution scheme. Thus, from the linearization of Eqs. (57) and (59), respectively one obtains

$$f_{p_i}^{(k)} + \mathbf{n}_i^{(k)\mathrm{T}} \delta\sigma^{(k)} + f_{p_i,\kappa_i}^k c_i^{(k)} \delta\lambda_{p_i}^{(k)} = 0, \quad 0 < i \leq 2 \tag{61}$$

and

$$\mathbf{r}^{(k)} + \delta\sigma^{(k)} + \mathbf{E} \sum_{j=1}^{N=2} \Delta\lambda_{p_j}^{(k)} \mathbf{H}_j^{(k)} \delta\sigma^{(k)} + \mathbf{E} \sum_{j=1}^{N=2} \delta\lambda_{p_j}^{(k)} \mathbf{m}_j^{(k)} = 0 \tag{62}$$
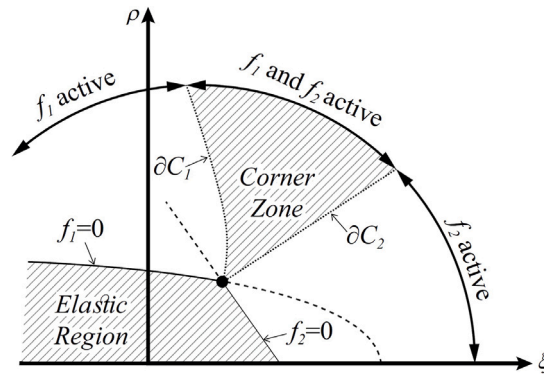
**Fig. 1.** Two surface model in Rendulic plane.

where Eq. (3) was used in iterative–incremental form, i,e, $\delta\kappa_{p_i} = \delta\lambda_{p_i}c_{p_i}$. Solving for $\delta\boldsymbol{\sigma}^{(k)}$ from Eq. (62) produces

$$\delta\boldsymbol{\sigma}^{(k)} = -\mathbf{Q}^{-1}\left(\mathbf{r}^{(k)} + \mathbf{E}\sum_{j=1}^{N=2}\delta\lambda_{p_j}^{(k)}\mathbf{m}_j^{(k)}\right) \tag{63}$$

Substituting Eq. (63) into Eqs. (61) produces the vector of proportionality factors as in Eq. (44), i.e.,

$$\delta\boldsymbol{\lambda}^{(k)} = \begin{Bmatrix} \delta\lambda_{p_1}^{(k)} \\ \delta\lambda_{p_2}^{(k)} \end{Bmatrix} \tag{64}$$

The solutions of $\delta\lambda_{p_i}^{(k)}$ are then used in Eq. (42) to update the plastic strain increment within the current step $(n+1)$. On the other hand, to implement the Cutting Plane Algorithm as a special case, one needs to assume that the residual vector $\mathbf{r}^{(k)}$ in Eq. (59) a-priori vanishes and $\mathbf{R} = \mathbf{E}$ in all iterations, which bypasses the need for the calculation of the Hessian matrix $\mathbf{H}_i$ of the active surfaces in Eq. (50), which might be difficult to obtain analytically if the potential surface function is complicated. Nevertheless, the potential surfaces function adopted in this study conveniently vanishes, i.e. $\mathbf{R} = \mathbf{E}$ is valid also for the Closest-Point Projection Algorithm by virtue of the concrete material model adopted in Section 4 due to the fact that selected potential functions are low order. Thus, which of the algorithms used in this study is only a matter of whether the vanishing of the residual vector $\mathbf{r}^{(k)}$ is adopted as a condition or not.

It is also important to note that to obtain a unique solution for $\delta\boldsymbol{\lambda}^{(k)}$ from Eq. (44), the matrix $\mathbf{A}^{(k)}$ should be invertible. In associative perfect plasticity, the uniqueness conditions are automatically met. For the case with associative plasticity with hardening, hardening-related terms enforce a limit on uniqueness of the solution (see [51]). On the other hand, for the general case, where plastic flow is non-associative and hardening takes place, the uniqueness of the solution relies on all terms of the matrix $\mathbf{A}^{(k)}$. For the matrix $\mathbf{A}^{(k)}$ to be invertible, the conditions can be written as

$$a_{11}^{(k)} > 0, \quad a_{22}^{(k)} > 0, \quad \det(\mathbf{A}^{(k)}) = |\mathbf{A}^{(k)}| = a_{11}^{(k)}a_{22}^{(k)} - a_{12}^{(k)}a_{21}^{(k)} > 0 \tag{65}$$

in which the first two conditions are related to the single-surface plasticity while the third condition arises when both surfaces are active. If any of the three conditions in Eq. (65) is not satisfied due to the fact that $f_{p_1,\kappa_1}^k c_1^{(k)} < 0$ or $f_{p_2,\kappa_2}^k c_2^{(k)} < 0$ in the softening regions, then we assign $f_{p_1,\kappa_1}^k c_1^{(k)} = 0$ and/or $f_{p_2,\kappa_2}^k c_2^{(k)} = 0$, where necessary to prevent premature convergence failures.

### 3.2. Return mapping in haigh–westergaard coordinates

As we adopt isotropic material assumption, we will use Haigh–Westergaard coordinates for its convenience. Fig. 1 depicts a generic two surface model in Rendulic plane, where $\xi$ is a measure of the volumetric component of the stress state and $\rho$ is a measure of deviatoric component of the stress state, i.e.

$$\xi = \frac{1}{\sqrt{3}f_c}\,\mathrm{tr}(\boldsymbol{\sigma}) \tag{66}$$

$$\rho = \frac{\sqrt{2J_2}}{f_c} \tag{67}$$

Haigh–Westergaard coordinates are related to the principal stress components as

$$\begin{Bmatrix} \sigma_1 \\ \sigma_2 \\ \sigma_3 \end{Bmatrix} = \frac{1}{\sqrt{3}}\begin{Bmatrix} \xi \\ \xi \\ \xi \end{Bmatrix} + \sqrt{\frac{2}{3}}\rho\begin{Bmatrix} \cos\theta \\ \cos\left(\theta - \frac{2\pi}{3}\right) \\ \cos\left(\theta + \frac{2\pi}{3}\right) \end{Bmatrix} \tag{68}$$

in which $\theta$ is the Lode angle that defines the orientation according to the polar coordinate system within the deviatoric plane of the Haigh–Westergaard space. For further details about Haigh–Westergaard coordinate system one is referred to [35]. The Lode angle $\theta$ is related to the deviatoric stress tensor components as

$$\cos 3\theta = \frac{3\sqrt{3}}{2} \frac{J_3}{J_2^{3/2}} \tag{69}$$

In Eqs. (67), (69) and (71), the following stress tensor invariants have been used.

$$\sigma_V = \frac{I_1}{3} = \frac{1}{3}\operatorname{tr}(\sigma)$$

$$J_2 = \frac{1}{2}\operatorname{tr}\left(s^2\right)$$

$$J_3 = \frac{1}{3}\operatorname{tr}\left(s^3\right) = \det(s) \tag{70}$$

in which tr() is the trace operator, $\sigma_V$ is the volumetric stress and $s$ is the deviatoric stress components of the stress tensor $\sigma$, i.e.

$$s = \sigma - \sigma_V \delta \tag{71}$$

where $\delta$ is the Kronecker's delta

$$\delta_{ij} = \begin{cases} 1, & i = j \\ 0, & i \neq j \end{cases} \tag{72}$$

### 3.2.1. Material parameters in terms of Bulk and Shear Moduli

By virtue of the material model selected in Section 4, the matrix $\mathbf{A}$ used in Eq. (44) for plastic stress return calculations can be conveniently expressed in terms of the bulk and shear moduli. For the alternative expression of $\mathbf{A}$, we first refer to the elastic stress due to elastic strain. From Eq. (71), one obtains

$$\sigma = s + \sigma_V \delta = \mathbf{E} : \varepsilon = 3K\epsilon_V \delta + 2Ge \tag{73}$$

where

$$K = \frac{E}{3(1 - 2\nu)} \tag{74}$$

and

$$G = \frac{E}{2(1 + \nu)} \tag{75}$$

written above in terms of the Elasticity Modulus $E$ and Poisson's ratio $\nu$ and in Eq. (73), volumetric strain

$$\epsilon_V = \frac{\operatorname{tr}(\varepsilon)}{3} \tag{76}$$

and deviatoric strain

$$e = \varepsilon - \epsilon_V \delta \tag{77}$$

definitions were used. From the definition in Eqs. (73) to (77), one obtains the relation

$$\sigma_V = 3K\epsilon_V \tag{78}$$

$$s = 2Ge \tag{79}$$

Note that for shear stress–shear strain relations in Voigt vector notation Eq. (79) should be evaluated as

$$\tau = G\gamma \tag{80}$$

Note that the relations between shear strain and stress are expressed differently in tensor and vector notations. In vector notations the shear strain components are $\gamma = 2e$, in which $e$ refers to the last three components of the six dimensional deviatoric strain tensor. Thus, shear strains should be treated with caution in numerical calculations. By using Eqs. (68), (78) and (79), we can write $f_{p,\sigma}{}^{\mathrm{T}}\mathbf{E}g_{p,\sigma}$ alternatively as

$$f_{p_i,\sigma}{}^{\mathrm{T}}\mathbf{E}g_{p_i,\sigma} = 3Kf_{p_i,\xi}g_{p_i,\xi} + 2Gf_{p_i,\rho}g_{p_i,\rho} + \frac{2G}{\rho^2}f_{p_i,\theta}g_{p_i,\theta} \quad , 0 < i \leq 2 \tag{81}$$

from which by substituting into Eq. (45), one obtains

$$\mathbf{A}^{(0)} = \begin{bmatrix} 3Kf^0_{p_1,\xi}g^0_{p_1,\xi} + 2Gf^0_{p_1,\rho}g^0_{p_1,\rho} + f^0_{p_1,\kappa_1}c^0_1 & 3Kf^0_{p_1,\xi}g^0_{p_2,\xi} + 2Gf^0_{p_1,\rho}g^0_{p_2,\rho} \\ 3Kf^0_{p_2,\xi}g^0_{p_1,\xi} + 2Gf^0_{p_2,\rho}g^0_{p_1,\rho} & 3Kf^0_{p_2,\xi}g^0_{p_2,\xi} + 2Gf^0_{p_2,\rho}g^0_{p_2,\rho} + f^0_{p_2,\kappa_2}c^{(0)}_2 \end{bmatrix} \tag{82}$$

where $g_{p_i,\theta} = 0$ for $0 < i \leq 2$ was used to eliminate the last term in Eq. (81). In Eq. (82), the superscript indicates the initial iteration, i.e., $(k) = 0$. We have obtained Eq. (82) for the initial iteration for the purpose of identifying the target yield surface. As we will discuss next, in our algorithm we select the return surface at the initial iteration based on Eq. (82), after which the procedure explained in Section 3.1 above, is used to update the stresses. It should be noted that $f_{p,\sigma}$ and $g_{p,\sigma}$ are generally tensors, however, all terms on the right hand side of Eq. (81), e.g. $f_{p,\xi}$, are conveniently scalar quantities which are provided in Section 4.

It is interesting to note that as a result of the selected potential function the corrective stress terms in Eq. (58) are independent of the Lode angle $\theta$. That is because, the plastic return strains, i.e., $\delta\varepsilon_{p_{(n+1)}}^{(k)}$ in Eq. (42) are independent of the Lode angle $\theta$. However, during plastic return process, unless the Poisson's ratio is zero the stresses drift from the Rendulic plane, which is initially determined based on the orientation of the trial stresses. It can be verified from Eq. (73) that only when the Poisson's ratio $\nu = 0$, the elastic stress tensor would become a scaling of the strain tensor with the Elasticity Modulus $E$, and thus, the corrected stresses in Eq. (63) would have the same directions with the plastic strains. However, in general $\nu \neq 0$ and therefore, there is a drift from the Rendulic plane of the trial stress, i.e. $\theta_{(n+1)} \neq \theta_{(n+1)}^{\text{trial}}$.

### 3.3. Four possible scenarios of the return algorithm

When both surfaces are active we refer to it as the first scenario, which is when the non-converged stresses are in the corner zone region of the stress space. On the other hand, during the return mapping process at the intermediate iterations, if the stress state is outside of the corner zone, then it yields to the classical single-surface plasticity problem. When only the first surface is active, we refer to it as the second scenario and when only the second surface is active we refer to it as the third scenario. Finally, when no surface is active and thus, the stress is in the elastic region, we refer to it as scenario zero. In Fig. 1, the boundaries between corner zone and single-surface zones are denoted with the symbols $\partial C_1$ and $\partial C_2$ on both sides. In the following, we introduce the criteria for the selection of the active surface. Note that the Cutting Plane and Closest Point Projection Algorithms are identical for the initial iteration. In our algorithm, we do not change the targeted yield surface during the iterations of return mapping despite the fact that at intermediate stages of the return process, the stresses may fall out of the initially selected zone. This possibility have been reported in literature e.g., [43]. If at the end of the return process any of the yield conditions is still violated, then another round of return process is triggered. If another round is triggered the trial stresses at the initial iteration of the current round is taken as the stress of the final iteration of the previous round as in Fig. 2.

#### 3.3.1. Scenario 1 - both surfaces are active

When both surfaces are active at the initial iteration, the Kuhn–Tucker conditions given in Eq. (5) for $M = 2$ produces

$$
\begin{aligned}
f_1^0 &> 0, \quad \delta\lambda_1^0 > 0 \\
f_2^{\,0} &> 0, \quad \delta\lambda_2^0 > 0
\end{aligned}
\tag{83}
$$

It should be noted that Eq. (83) is implemented in a finite incremental fashion therefore, before convergence is achieved both yield conditions are violated which makes the surfaces active during the iterations. As mentioned above, we select the scenario to implement out of the four possible scenarios after evaluating the yield surface values of the initial iteration, i.e. $f_i^0 > 0$. On the other hand, from, Eq. (44), requirement of a solution for positive proportionality factors, i.e., $\delta\lambda_i^0 > 0$, produces

$$
\begin{aligned}
\delta\lambda_1^0 &= \frac{a_{22}^0 \delta b_1^0 - a_{12}^0 \delta b_2^0}{|\mathbf{A}^0|} \\
\delta\lambda_2^0 &= \frac{-a_{21}^0 \delta b_1^0 + a_{11}^0 \delta b_2^0}{|\mathbf{A}^0|}
\end{aligned}
\tag{84}
$$

From Eq. (84), the criteria to activate Scenario 1 can be obtained as

$$
\begin{aligned}
a_{22}^0 f_1^0 &\geq a_{12}^0 f_2^0 \\
a_{11}^0 f_2^0 &\geq a_{21}^0 f_1^0
\end{aligned}
\tag{85}
$$

which are in addition to the uniqueness conditions provided in Eq. (65) and violation of yield conditions in Eq. (83) for the initial iteration. It is also interesting to note that as can be seen from Fig. 1, when both surfaces are active there is only one return point within the corner zone that satisfies both yield conditions. Therefore, the corner return point is not affected by whether the algorithm is Closest-Point-Projection or Cutting-Plane.

#### 3.3.2. Scenario 2 - only surface 1 is active

When only the first surface is active at the initial iteration, the Kuhn–Tucker conditions given in Eq. (5) produces

$$
\begin{aligned}
f_1^0 &> 0, \quad \delta\lambda_1^0 > 0 \\
f_2^{\,0} &= 0, \quad \delta\lambda_2^0 = 0
\end{aligned}
\tag{86}
$$

From, Eq. (44) requirement of a solution for positive proportionality factor for $i = 1$, i.e., $\delta\lambda_1^0 > 0$, produces

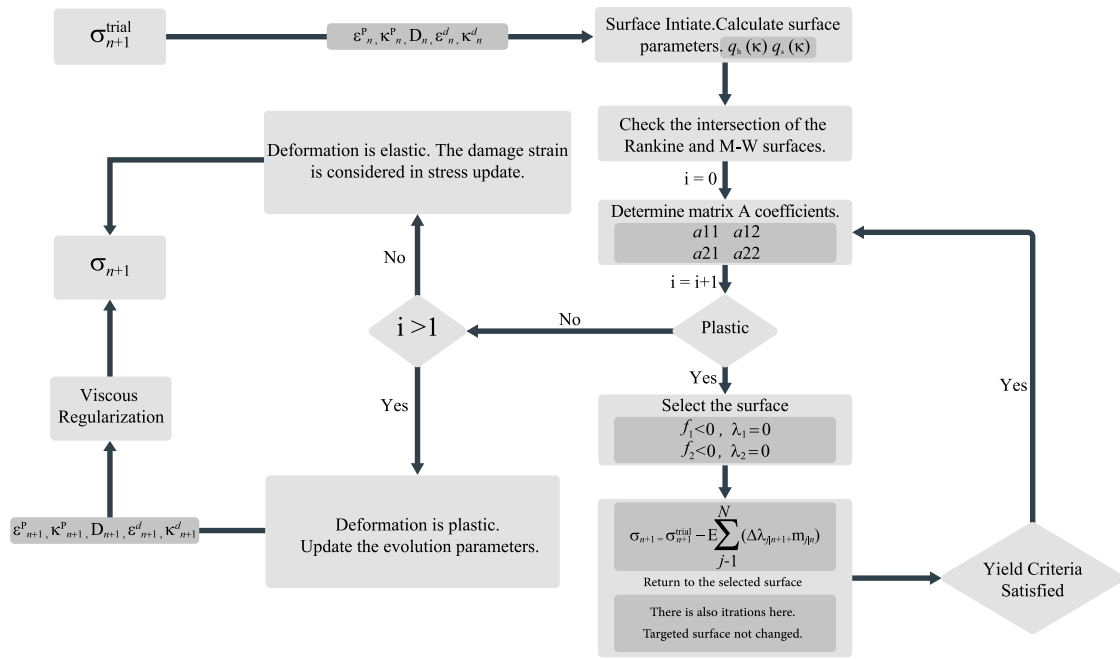$$
a_{22}^0 f_1^0 \geq a_{12}^0 f_2^0
\tag{87}
$$

**Fig. 2.** Return mapping algorithm.

$$a_{21}^0 f_1^0 > a_{11}^0 f_2^0 \tag{88}$$

It is also interesting to note that, in this case the return point is affected by whether the algorithm is Closest-Point Projection or Cutting-Plane.

### 3.3.3. Scenario 3 - only surface 2 is active

For when only the second surface is active, the Kuhn–Tucker conditions produces

$$f_2^0 = 0, \quad \delta\lambda_1^0 = 0$$
$$f_1^0 > 0, \quad \delta\lambda_2^0 > 0 \tag{89}$$

From, Eq. (44) requirement of a solution for positive proportionality factor for $i = 2$, i.e., $\delta\lambda_2^0 > 0$, produces

$$a_{12}^0 f_2^0 > a_{22}^0 f_1^0 \tag{90}$$

$$a_{11}^0 f_2^0 \geq a_{21}^0 f_1^0 \tag{91}$$

### 3.3.4. Scenario 0 - No surface is active

When the Kuhn–Tucker conditions at initial iterations are such that

$$f_1^0 < 0, \quad \delta\lambda_1^0 = 0$$
$$f_2^0 < 0, \quad \delta\lambda_2^0 = 0 \tag{92}$$

then there is no active surface and we accept the trial stress as the final stress within the incremental step $(n + 1)$.

### 3.4. Damage compliance matrix

Based on $\mathbf{Y}$ introduced in Eq. (32), the Damage Compliance can be written in matrix form as

$$\mathbf{D} = \left[ \phi \mathbf{E}^{-1} + \omega \varepsilon_p \varepsilon_p^T \mathbf{E}^{-1} \right] \tag{93}$$

where $\varepsilon_p$ is now a column vector. Note that $\mathbf{DE}$ takes a symmetrical form. From Eq. (31), i.e. $\mathbf{DE}\varepsilon_p = (\phi + \omega\chi)\varepsilon_p$, where $\chi = \varepsilon_p^T \varepsilon_p$, one obtains $\bar{\phi} = \phi + \omega\chi$. It is also interesting to note that the anisotropic damage compliance term, i.e. $\mathbf{Y}$ in Eq. (93) is a rank-1

matrix. An example of the use of rank-1 anisotropic damage compliance matrix can be found in [12]. From Eq. (93), and by using Sherman–Morison–Woodbury formula in the relation $\mathbf{M} = (\mathbf{I} + \mathbf{ED})^{-1}$, one obtains

$$\mathbf{M} = \frac{1}{1+\phi}\left[\mathbf{I} - \gamma\mathbf{E}\boldsymbol{\varepsilon}_p\boldsymbol{\varepsilon}_p^T\mathbf{E}^{-1}\right] \tag{94}$$

in which $\gamma = \frac{\omega}{(1+\phi+\omega\chi)}$. Again, by using the Sherman–Morison–Woodbury formula in Eq. (93), one obtains the inverse of the damage tensor as

$$\mathbf{D}^{-1} = \phi^{-1}\mathbf{E}\left[\mathbf{I} - \beta\boldsymbol{\varepsilon}_p\boldsymbol{\varepsilon}_p^T\right] \tag{95}$$

in which $\beta = \frac{\omega}{(\phi+\omega\chi)}$. By using Eq. (95) and substituting into Eq. (20), one obtains

$$\bar{\phi} = \frac{\boldsymbol{\varepsilon}_p^T : \mathbf{E} : \boldsymbol{\varepsilon}_p}{(\phi^{-1} - \phi^{-1}\beta\chi)\boldsymbol{\varepsilon}_p^T : \mathbf{E} : \boldsymbol{\varepsilon}_p} = \frac{\phi}{1-\beta\chi} \tag{96}$$

From Eqs. (93) and (94), by using $\mathbf{P} = \mathbf{DME}$, one obtains

$$\mathbf{P} = \frac{1}{1+\phi}\left[\phi\mathbf{I} + \gamma\boldsymbol{\varepsilon}_p\boldsymbol{\varepsilon}_p^T\right] \tag{97}$$

By using the relation $\phi = \varphi/(1 - \varphi)$ in Eq. (97), one obtains.

$$\mathbf{P} = \left[\varphi\mathbf{I} + (1-\varphi)\gamma\boldsymbol{\varepsilon}_p\boldsymbol{\varepsilon}_p^T\right] \tag{98}$$

We use Eq. (98) in Eq. (39) to introduce damage update to the stress state, when the trial stress is elastic. On the other hand, matrix $\mathbf{P}$ is updated according to the plastic strains, further details of which are provided according to the material type under Section 4.

### 3.5. Viscous regularization

The viscous behaviour can be considered as a modification to the values obtained after the above time integration algorithm described based on the rate-independent plasticity assumption. This approach is often referred to as Duvaut and Lions model (see [20]), in which the final value of stresses as well as hardening parameters are expressed as a linear combination of the trial elastic value and the converged stress of the rate independent algorithm, where the weighting factors are functions of the time step and the retardation time. Introducing viscous effects improves the numerical stability which may be required in the case of strain softening (see [51]). According to Duvaut and Lions model, the updated stress and evolution parameters can be written as

$$\boldsymbol{\sigma}_{(n+1)}^{final} = \boldsymbol{\sigma}_{(n)}e^{-\psi\Delta t} + \boldsymbol{\sigma}_{(n+1)}(1 - e^{-\psi\Delta t}) + \frac{(1 - e^{-\psi\Delta t})}{\psi\Delta t}\mathbf{E}\Delta\boldsymbol{\varepsilon}_{(n+1)} \tag{99}$$

and

$$\kappa_i^{final} = \kappa_{i_{(n)}}e^{-\psi\Delta t} + \kappa_{i_{(n+1)}}(1 - e^{-\psi\Delta t}) \tag{100}$$

in which $\psi = 1/\tau$, where $\tau$ is the retardation time and $\Delta t$ is the time increment of the step. The retardation time is a viscosity related material property which refers to the necessary time for complete stress relaxation to the final state. Thus, under the rate independent plasticity assumption of no relaxation, i.e., $\tau \to 0$, for any $\Delta t$, Eqs. (99) and (100) regenerate $\boldsymbol{\sigma}_{(n+1)}$ and $\kappa_{i_{(n+1)}}$, respectively, which are the last converged values of the rate-independent plasticity algorithm described above. It will be shown in case studies that by selecting a positive value for $\psi\Delta t$, the numerical stability of the algorithm can be improved. We also adopt the formulation to update the damage matrix, i.e.

$$\mathbf{P}_i^{final} = \mathbf{P}_{i_{(n)}}e^{-\psi\Delta t} + \mathbf{P}_{i_{(n+1)}}(1 - e^{-\psi\Delta t}) \tag{101}$$

The complete flow chart of the developed procedure is provided in Fig. 2.

## 4. Specifics of the material model

Concrete is a pressure-sensitive material, and its responses to compressive and tensile loads are considerably different. In particular, under uniaxial tensile load, tensile cracks start to form perpendicular to the dominant tensile stress and they can coalesce to form larger cracks. Consequently, when the tensile strength is reached, the loss of strength is observed in the form of rapid softening in the stress–strain curve. Furthermore, the presence of tensile cracks also causes degradation in material moduli. To reflect these characteristics of concrete in the plastic-damage constitutive modelling, softening is generally simulated through the evolution of yield criteria, and degradation of material moduli is captured by the use of damage variables. On the other hand, under uniaxial compression loading, the inelastic response of concrete is generally manifested by compression cracks that commonly develop parallel to the compressive stress direction. Tangential stiffness reduces as the material is pushed further to its elastic limit, and the compression stress reaches to its maximum value at the compressive strength. Under persistent loading, a softening regime follows. Similar to the tensile case, material moduli also degrade as a result of inelastic processes. When multiaxial loading takes place, concrete's behaviour can change significantly, especially for the triaxial compressive loading. As the confining pressure increases, the strength and ductility of concrete grows significantly. It is important to reflect this characteristic of concrete in constitutive models

where confinement pressure can become significant. Due to the reasons explained above, Rankine-type yield surfaces (which are triangular in the deviatoric plane) are common in tensile modelling whereas Drucker–Prager type yield surfaces (which are round in the deviatoric plane) provide better performance in compressive modelling of concrete because of their pressure dependency, however, it does not account for the intermediate principal stress in failure. The yield surface proposed by [4] is commonly adopted for the simulation of concrete also considers the intermediate principal stresses in compression failure, which is an extension of the Drucker–Prager type failure criterion. It is also common to use a set of yield criteria simultaneously (e.g., Rankine for tension and Drucker–Prager type for compression) to capture compressive and tensile characteristics more accurately. This multi-surface approach also allows the use of different damage evolutions in tension and compression, offering more control on the model for capturing the actual behaviour.

### 4.1. Menetrey–Willam surface for concrete compression

The yield surfaces are described in terms of Haigh–Westergaard in stress space. Haigh–Westergaard coordinates are $(\xi, \rho, \theta)$, where $\xi$ is the hydrostatic stress invariant, $\rho$ is the deviatoric stress invariant, $\theta$ is the deviatoric polar angle as described in Section 3.2. The yield surface proposed by [4] is given by the following equation:

$$f_{p_1}(\xi, \rho, \theta) = 1.5 \left( \frac{\rho}{f_c} \right)^2 + q_h(\kappa_p) m \left( \frac{\rho}{f_c \sqrt{6}} r + \frac{\xi}{f_c \sqrt{3}} \right) - q_h(\kappa_p) q_s(\kappa_p) \leq 0 \tag{102}$$

where $f_c$ is the uniaxial compressive strength. In Eq. (102), $m$ is introduced as a measure of frictional strength in [4] and it can be written as

$$m = 3 \frac{f_c^2 - f_t^2}{f_c f_t} \frac{e}{e+1} \tag{103}$$

in which $f_t$ is the uniaxial tensile strength and $e$ is called eccentricity which describes the out-of-roundness of the yield surface in the deviatoric plane (see Fig. 3) i.e.

$$e = \frac{1 + \epsilon}{2 - \epsilon} \tag{104}$$

where

$$\epsilon = \frac{f_t}{f_b} \frac{f_b^2 - f_c^2}{f_c^2 - f_t^2} \tag{105}$$

In Eq. (102), $r$ is the radius in the deviatoric plane which is a function of the deviatoric polar angle $\theta$ and the eccentricity $e$ i.e.

$$r(\theta, e) = \frac{\upsilon(\theta, e)}{s(\theta, e) + t(\theta, e)} \tag{106}$$

where

$$\upsilon(\theta, e) = 4 \left( 1 - e^2 \right) \cos^2 \theta + (2e - 1)^2 \tag{107}$$

$$s(\theta, e) = 2 \left( 1 - e^2 \right) \cos \theta \tag{108}$$

$$t(\theta, e) = (2e - 1) \left[ 4 \left( 1 - e^2 \right) \cos^2 \theta + 5e^2 - 4e \right]^{1/2} \tag{109}$$

### 4.1.1. Hardening and softening functions

We adopt an isotropic hardening law based in which the hardening and softening functions are $q_h$ and $q_s$ respectively. Thus, only the size of the yield surface change, which is controlled by the hardening/softening parameter $\kappa_{p_1}$. Following [6], we select the hardening parameter to be the plastic volumetric strain $\varepsilon_v^p$. i.e.

$$d\kappa_{p_1} = d\varepsilon_v^p = d\lambda_p \frac{\sqrt{3}}{q_h q_s} \tag{110}$$

The function $q_h$ is active in the hardening region and it is unity beyond the peak strain whereas $q_s$ is active in the softening region. According to the hardening law in [6] (see Fig. 4), the hardening function in Eq. (102) can be written as

$$q_h \left( \kappa_{p_1} \right) = q_h \left( \varepsilon_v^p \right) = k_o + (1 - k_o) \sqrt{1 - \left( \frac{\varepsilon_{vo}^p - \varepsilon_v^p}{\varepsilon_{vo}^p} \right)^2} \tag{111}$$
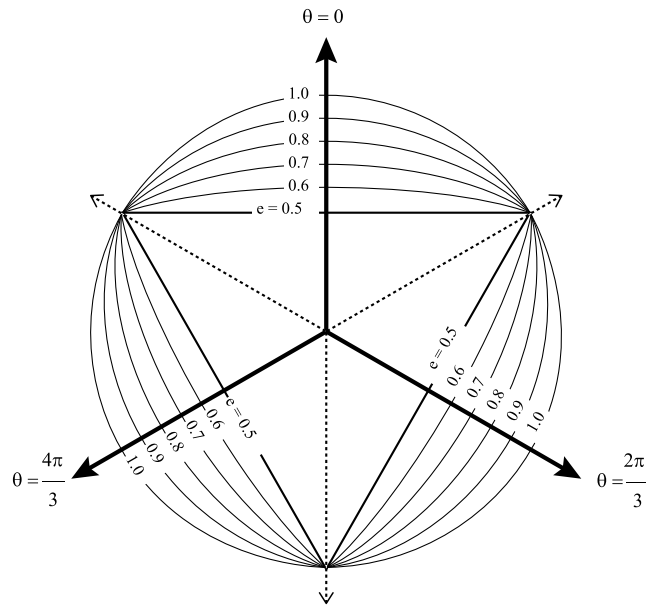
where

$$k_o = \sigma_{c_o} / f_c \tag{112}$$

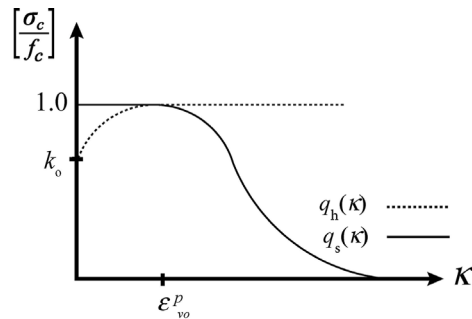**Fig. 3.** Deviatoric plane of the yield surface.



**Fig. 4.** The split of hardening function into the hardening and softening part.

in which $\sigma_{c_o}$ is the uniaxial concrete stress at the onset of plastic flow. In Eq. (111), $\varepsilon_{vo}^p$ is the threshold value for the volumetric plastic strain at uniaxial concrete strength, i.e.

$$\varepsilon_{vo}^p = \frac{f_c}{E_c}(1 - 2\nu_c) \tag{113}$$

where $E_c$ and $\nu_c$ are the Young's modulus and Poisson ratio for concrete, respectively.

$$q(\kappa_{p_1}) = q_h(\kappa_{p_1})q_s(\kappa_{p_1}) \tag{114}$$

The softening function $q_s$ is unity during the hardening range and its value is updated only beyond the peak compressive strain, i.e.

$$q_s\left(\kappa_{p_1}\right) = \left(\frac{1}{1 + \left(\frac{n_1 - 1}{n_2 - 1}\right)^2}\right)^2 \tag{115}$$

where

$$n_1 = \frac{\varepsilon_v^p}{\varepsilon_{vo}^p} \tag{116}$$

and

$$n_2 = \frac{\varepsilon_{vo}^p + t_c}{\varepsilon_{vo}^p} \tag{117}$$

in which $t_c$ is a calibrated parameter and considering MPa as the stress unit, it is recommended to use $t_c = f_c/15000$ (see [38]).

## 4.2. Potential function for concrete compression

We adopt the linear potential function proposed in [11], which can be expressed in Haigh–Westergaard coordinates as

$$g_{p_1}(\xi, \rho) = -B\rho + \xi - a \tag{118}$$

where $B$ controls the slope in Rendulic Plane and it is chosen to give proper dilatancy. In [11] a value between $-6.6$ and $-5$ is suggested in their case studies, which we adopt herein. The effect of slope $B$ will be shown in Section 6 case studies. It should be noted that more sophisticated potential functions that describe the confined concrete behaviour more accurately can be found in literature e.g. [6,38], which may cause some differences in results when the concrete is confined. However, in our experience the linear potential function selected herein performs well in numerical simulations as will be shown in Section 6, while other alternatives may cause convergence issues especially when tensile stresses are involved. It should also be noted that as we use the gradient of the potential function and not the potential function value itself, the value of $a$ in Eq. (118) has no influence in the derivation of equations and results. It is a constant introduced to adjust the position of the potential function to be meaningful, i.e., to meet with the point of current stress state.

## 4.3. Rankine surface for concrete tension

In tensile region, we also adopt non-associative flow rule to be able to use a potential function that is independent of the polar angle $\theta$, while using the Rankine yield surface to limit the maximum stress at the tensile strength. In Haigh–Westergaard coordinates the Rankine surface can be written as

$$f_{p_2}(\xi, \rho, \theta) = \sqrt{2}\rho \cos\theta + \xi - \sqrt{3}f_t \tag{119}$$

On the other hand, the potential function is obtained by removing the dependence to angle $\theta$ in Eq. (119) as

$$g_{p_2}(\xi, \rho) = \sqrt{2}\rho + \xi - b \tag{120}$$

By adopting the potential function in Eq. (120), we assure that the condition $g_{p_2,\theta} = 0$, which was used in the derivation of Eq. (82) is valid in the tension zone. Similar to the compressive potential surface constant $a$, the value of $b$ in Eq. (120) has no influence in the derivation of the equations.

## 4.4. Evolution of the damage for concrete

The damage parameter $\varphi$, is updated based on the volumetric plastic strain proposed for concrete material in [17], i.e.

$$\varphi = \left(1 - e^{-C\frac{\kappa_p}{\epsilon_{vo}^p}}\right) \tag{121}$$

where $C$ is a parameter to be calibrated based on cyclic tests. It should be noted that the same damage function in Eq. (121) is used for both compressive and tensile behaviour of concrete, however, their calibration parameters $C$ are adjusted differently. On the other hand, the coefficient $\omega$ is used to calibrate the anisotropic component in Eq. (98). The coefficient $\gamma$ in Eq. (98) can be updated according to the evolution of $\varphi$, i.e.

$$\gamma = \frac{(1 - \varphi)\omega}{1 + (1 - \varphi)\omega\chi} \tag{122}$$

in which $\chi = \varepsilon_{p_{(n)}}^T \varepsilon_{p_{(n)}}$ is calculated based on the last converged plastic strain update.

## 4.5. Material model for the steel reinforcement bars

The uniaxial material model for the reinforcement is based on a relatively simpler yield function for the steel material, i.e.

$$f_r(\sigma_r, \kappa_r) = |\sigma_r| - (\sigma_y + \kappa_r) \tag{123}$$

where $\sigma_r$ is the axial stress acting on the integration points of the cross-section of the reinforcement bars, $\sigma_y$ is the yield stress limit for the steel material and $\kappa_r$ is the hardening modulus for steel. The plastic hardening function which is assumed a linear function of the plastic proportionality factor as

$$d\kappa_r = d\lambda_r K_r \tag{124}$$

where $K_r(\sigma_r, d\lambda_r)$ is the corresponding hardening modulus for the steel material. Due to the uniaxial stress state, the return mapping of the axial stress to the yield surface is a special case of the algorithm introduced in Section 3. Thus, the return mapping of the trial stress at the current step $\sigma_{r_{(n+1)}}^{\text{trial}}$, on to the yield surface is a matter of simple scaling i.e.

$$\sigma_{r_{(n+1)}}^{\text{trial}} = \sigma_{r_{(n)}} + E_r \Delta\varepsilon_{r_{(n+1)}} \tag{125}$$

where $\sigma_{r(n)}$ is the last converged bar stress, $E_r$ is the elasticity modulus of the steel material and $\Delta\varepsilon_{r(n+1)}$ is the total strain increment of the reinforcement bar within the current step $(n + 1)$. We would like to note that in order to be able to have variety in the applications, e.g. cases of metal fatigue etc., we keep the damage terms also for the rebars. Accordingly, if the trial stress on the rebar is within the yield surface limits, then the final stress considering the existing damage state can be written as

$$\sigma_{r(n+1)} = \sigma_{r(n)} + \frac{E_r}{1 + \phi_r} \Delta\varepsilon_{r(n+1)} \tag{126}$$

where $\phi_r$ is the damage parameter for the steel material at the last converged step. Exponential damage evolution is also often assumed for the steel material (see [52]). Reduction of the elasticity modulus under cyclic loading based on an exponential function of similar form was also proposed in several works e.g., [53,54]. Therefore, for the steel reinforcement, we also adopt Eq. (121) by replacing $\kappa_p/\epsilon_{vo}^p$ in Eq. (121) with $\kappa_r$, for which the parameter $C$ should be calibrated specifically for the reinforcement behaviour.

## 5. Solution of the global equilibrium equations

### 5.1. Variational form of the equilibrium equations

To generate the finite element solution, we first start with the general equilibrium equations based on the principle of virtual work i.e.,

$$\delta\Pi = \delta W^{int} - \delta W^{ext} = 0 \tag{127}$$

where $\delta W^{int}$ is the variation of the internal work, i.e.,

$$\delta W^{int} = \int_V \delta\varepsilon^T \sigma \, dV + \int_L \int_A \delta\varepsilon_r \sigma_r \, dA \, dL \tag{128}$$

in which, first term on the right-hand side is the contribution of the concrete bulk over the volume $V$, whereas the second term on the right-hand side is the contribution of the reinforcement bars over the span $L$ whose cross-sectional area is represented with $A$. Kinematic relations can be directly built between the variations of strains and the variations of nodal displacements as

$$\delta\varepsilon = B\delta d_e \tag{129}$$

and

$$\delta\varepsilon_r = s_r B_r \delta d_e \tag{130}$$

where $d_e$ is the element displacement vector and matrices $B$ and $B_r$ form the element level discretized strain–displacement relations, which depends on the selected finite element interpolation field. In Eq. (130), $s_r$ is a row vector of the generalized cross-sectional coordinates that imposes linear strain distribution over the cross-section based on the Euler–Bernoulli beam kinematics adopted for the rebars. The variation of strains for the beam-type rebar formulation is decomposed such that matrix $B_r$ is independent of the cross-sectional coordinates. Thus, by substituting Eq. (130) in to Eq. (128), and collecting the functions of cross-sectional coordinates of the rebar, we generate the expression $\int_A s_r^T \sigma_r \, dA$, which produces the vector of stress-resultants according to linear strain distribution across the section. That is, the stress-resultants of the rebar e.g., bending moment, axial force etc. are consistent with the kinematics of the Euler–Bernoulli beam theory. It should be noted that at the material level the elasto-plastic-damage material relationship is established between the axial strain and axial stress, which is the normal stress acting on the cross-section of the rebar. It should also be noted that for strain displacement relations, we have adopted geometrically linear small-strain assumption. In Eq. (127) $\delta W^{ext}$ is the virtual work done by the external loads, i.e.,

$$\delta W^{ext} = \delta d^T f^{ext} \tag{131}$$

where $f^{ext}$ is the vector of the external nodal forces and $\delta d$ is the vector of the displacement variations. In the finite element form, we refer to vector $\delta d$ as the nodal displacement vector. We adopt conventional displacement based finite element formulations with standard assemblage procedures. Therefore, the transition from element level vector and matrices to global level vector and matrices is a result of the standard assemblage procedure. For more details in standard finite element assemblage procedures see [55].

### 5.2. Linearization of the of equilibrium equations

Linearization of Eq. (127) produces

$$\delta d \cdot \nabla_d \delta\Pi = \int_V B^T C_{epd} B \, dV + \int_L B_r^T C_r B_r \, dL = \delta d^T K_{G_t} \delta d \tag{132}$$

Again, the transition from the element level vectors and matrices in Eq. (129) to the global level relations in Eq. (132) is a result of the standard assemblage procedure. In Eq. (132), $K_{G_t}$ denotes the tangent stiffness matrix and $\nabla_d$ is the gradient with respect to the nodal displacement vector. In Eq. (132), $C_{epd}$ is the material level tangent moduli for the concrete material, which can be obtained by substituting Eq. (7) into Eq. (11) and eliminating $d\varepsilon_d$, i.e.

$$C_{epd} = C_{ed} \left[ C_{ed} + C_{ep} \right]^{-1} C_{ep} \tag{133}$$

in which

$$\mathbf{C}_{ep} = \mathbf{E}\left[\mathbf{I} - \mathbf{m_b}\mathbf{A}^{-1}\mathbf{n_a}^{\mathbf{T}}\mathbf{E}\right] \tag{134}$$

where

$$\mathbf{n_a}^{\mathbf{T}} = \left\{ \begin{array}{c} \mathbf{n_1^T} \\ \mathbf{n_2^T} \end{array} \right\} \tag{135}$$

and

$$\mathbf{m_b}^{\mathbf{T}} = \left\{ \begin{array}{c} \mathbf{m_1^T} \\ \mathbf{m_2^T} \end{array} \right\} \tag{136}$$

were used and under the direct coupling assumptions in Eqs (13) to (22), one obtains $\mathbf{C}_{ed} = \mathbf{P}^{-1}\mathbf{C}_{ep}$. In deriving Eq. (133), the differential equations $d\lambda = \mathbf{A}^{-1}\mathbf{n_a}^{\mathbf{T}}\mathbf{E}d\varepsilon$, $d\varepsilon_p = \mathbf{m_b}$ and $d\lambda_{d_i} = \phi d\lambda_{p_i}$ were substituted into $d\boldsymbol{\sigma} = \mathbf{E}\left(d\varepsilon - d\varepsilon_p - d\varepsilon_d\right)$.

On the other hand, in Eq. (132), $\mathbf{C_r} = \int_A \mathbf{s_r}^{\mathbf{T}} E_{rpd} \mathbf{s_r} dA$ is a matrix of bar material and cross-sectional properties, in which for the elasto-plastic uniaxial steel material one obtains the tangent material modulus as

$$E_{rpd} = \frac{E_r K_r}{K_r \phi_r + E_r + K_r} \tag{137}$$

The Newton–Raphson solution of the non-linear equilibrium equation in Eq. (127) produces

$$\begin{bmatrix} \mathbf{K}_{G_t} & -\mathbf{f}^{ext} \\ \mathbf{a}^{\mathbf{T}(j)} & b^{(j)} \end{bmatrix} \left\{ \begin{array}{c} \delta\mathbf{d}^{(j)} \\ \delta\Lambda^{(j)} \end{array} \right\} = - \left\{ \begin{array}{c} \mathbf{r_d}^{(j)} \\ c^{(j)} \end{array} \right\} \tag{138}$$

where $\Lambda^{(j)}$ is a scaling factor that sets up the applied load level within each global iteration $(j)$ and $\mathbf{r_d}^{(j)}$ is the residual of the global equilibrium condition in Eq. (127) calculated at the end of each iteration. To solve the above augmented system of equations more efficiently the iterative displacement vector can be decomposed as

$$\delta\mathbf{d}^{(j)} = \delta\Lambda^{(j)}\delta\mathbf{d_p}^{(j)} + \delta\mathbf{d_r}^{(j)} \tag{139}$$

where $\delta\mathbf{d_p}^{(j)} = \mathbf{K}_{G_t}^{-1}\mathbf{f}^{ext}$ and $\delta\mathbf{d_r}^{(j)} = \mathbf{K}_{G_t}^{-1}\mathbf{r_d}^{(j)}$. From the second row of the augmented equation in Eq. (139) and using the displacement components, one obtains

$$\delta\Lambda^{(j)} = \frac{c^{(j)} - \mathbf{a}^{\mathbf{T}(j)}\delta\mathbf{d_r}^{(j)}}{\mathbf{a}^{\mathbf{T}(j)}\delta\mathbf{d_p}^{(j)}} \tag{140}$$

In Eqs. (139) and (140), the vector $\mathbf{a}^{(j)}$ and the constant $c^{(j)}$ enforces a constraint condition at each global iteration $(j)$, which allows selection of alternative control parameters while keeping the load scaling factor $\Lambda$ a variable. It should be noted that we solve the equations in an incremental–iterative manner, where we adopt a modified Newton–Raphson procedure and thus, update the stiffness matrix only at the beginning of the initial iteration. Therefore, $\mathbf{C}_{epd}$ and $E_{rpd}$, and accordingly $\mathbf{K}_{G_t}$ are presented without any reference to iteration $(j)$. However, they are updated after each converged increment. We have adopted the displacement control method to be able to trace the load–deflection curve beyond the peak strength. For the displacement-control method, the constraint conditions are such that the vector $\mathbf{a}^{(j)}$ is composed of zero components except a unity at the controlled degree-of-freedom and the constant $c^{(j)}$ takes the prescribed displacement value. To terminate the iterations in the global/finite element level solution, we have measured the ratio of the Euclid norm of each iterative increment in the displacement vector to the total increment in the displacement vector of the step. Further details on the displacement-control algorithm can be found in [56].

## 5.3. Finite element types for structural level modelling

For the analysis of structural components presented in the case studies, two types of elements are utilized. The elements are fully connected at their respective nodes. The concrete bulk is modelled using the 8-node solid element introduced in [57]. This element type is chosen for its capability to capture the complex three-dimensional stress states within the concrete material. The solid elements incorporate drilling degrees of freedom, which allow for the representation of rotational effects, maintaining a consistent 6-Degrees-Of-Freedom (6-DOFs) per node. The inclusion of rotational DOFs ensures that the solid elements are compatible with the beam elements used for the rebars. The integration scheme used for the solid elements is $3 \times 3 \times 3$. The standard two-node, 6-DOFs per node Euler–Bernoulli beam-bar elements are employed for the steel reinforcement. Thus, in-plane bending deformations are based on Hermitian interpolation whereas axial and twist deformations are based on linear interpolation, e.g. [55]. The torsional deformations induced by the loading are assumed negligible in comparison to axial deformations of the rebars. Therefore, the shear stress and shear strain relationships induced by the torsion are assumed to stay within the linear elastic range and are not involved in the return mapping of the axial trial stress. Thus, for the steel reinforcement bars, the elasto-plastic-damage material behaviour is established only between the axial stress and strains as explained in Section 4.5 and the effect of torsion induced shear stresses are neglected. Two Gauss integration points are used for the beam elements along their axis. The cross-sectional grids are taken as 4-by-4 where the integration points are taken at the centre of each grid segment. In all cases, the mesh is adjusted to generate nodes at the reinforcement locations so that the beam elements and solid elements are directly connected at the nodes. The implementation and assembly of these finite element types are carried out by developing a software using the Fortran programming language.
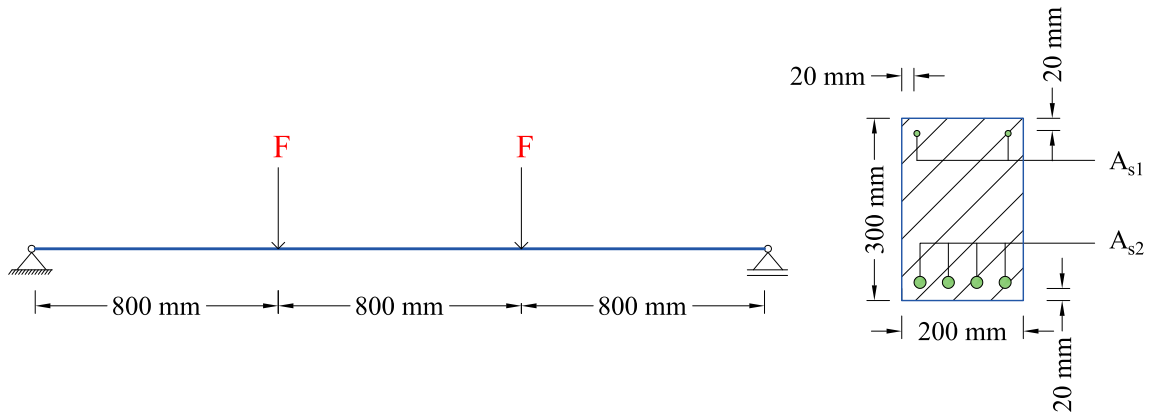
**Fig. 5.** Geometry, boundary conditions and loading of the beam.

**Table 1**
Material properties of the reinforced concrete beam.

| Material | Properties | Values | Unit |
|---|---|---|---|
| Concrete | Young modulus, $E_c$ | 29 730 | MPa |
| | Poisson ratio, $\nu$ | 0.2 | – |
| | Compression strength, $\sigma_c$ | 40 | MPa |
| | Tensile strength, $\sigma_t$ | 3.15 | MPa |
| | Strain at compression peak | 0.003 | – |
| | Strain at tensile peak | 0.0002 | – |
| Steel | Young modulus, $E_s$ | 210 000 | MPa |
| | Ultimate strength, $\sigma_y$ | 420 | MPa |
| | Compressive rebar section area, $A_{s1}$ | 1.02 | cm$^2$ |
| | Tension rebar section area, $A_{s2}$ | 4.52 | cm$^2$ |

## 6. Case studies

We consider three cases from the literature, referred in the following as four-point beam bending, eccentrically loaded column, and laterally loaded shear-wall, which are used to validate the developed tool. We introduce a fourth case to illustrate the differences in structural response under isotropic under anisotropic damage assumptions. For each case, we first introduce geometrical and material descriptions, loading and boundary conditions of the structural component. Secondly, we present the material specifications and analysis parameters used in the developed software and finally, we present the qualitative deformed shapes and load–deflection curves obtained from the developed software. It should be noted that only within the cross-sectional planes corresponding to the locations of applied external loads and boundary conditions, we impose Multiple-Point Constraints to avoid localized deformations and stress concentrations, absence of which was observed to create convergence problems. By the suggested application of Multiple-Point Constraints, we have managed to avoid convergence issues due to localizations and stress concentrations, and thus the presented results were obtained without interrupting the analysis procedure. To terminate iterations in both local material element level and global/finite level, we have introduced an error margin of maximum $10^{-4}$, i.e. in solving Eqs. (57) and (127). For the material level return-mapping, we have tested both the Cutting-Plane and the Closest-Point Projection algorithms. We have not observed any noticeable differences in the load–deflection curves. However, the Cutting-Plane algorithm generally required fewer iterations which in some cases significantly reduced the analysis time.

### 6.1. Four-point load beam bending test

The first case study is the four-point bending test of a simply-supported reinforced concrete beam presented in [41], which has an overall span of 2.4 m. The loading points are located at 0.8 meters and 1.6 meters from the end supports as shown in Fig. 5. The rectangular cross-section has a width of 200 mm and a height of 300 mm. The beam has no stirrups and it is reinforced with four longitudinal bars in tension and two in compression sides. The area of each of the tensile reinforcements is 4.52 cm$^2$ and the area of each of the compression reinforcements is 1.02 cm$^2$. The material properties of the concrete bulk and the steel reinforcements are provided in Table 1. The first numerical model is comprised of $6 \times 6$ element-mesh over the cross-section and 10-element mesh along the span resulting with 360 solid elements for the concrete bulk and in total of $6 \times 10 = 60$ beam elements for the reinforcements. Alternatively, we have used a 14-element mesh along the span resulting with 504 solid elements for the concrete bulk and in total of 84 beam elements for the reinforcements. The key analysis parameters used in the developed software are provided in Table 2.

**Table 2**

Parameters of the software for the four-point beam bending test.

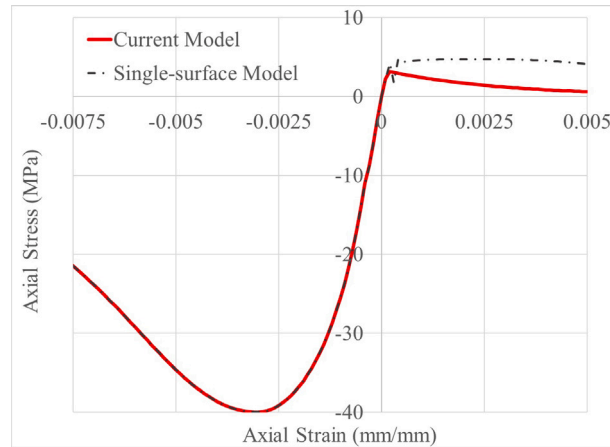| Parameters | Values | Units |
|---|---|---|
| Onset ratio plastic flow $k_o$ in Eq. (112) | 0.05 | – |
| Slope linear potential surface $B$ in Eq. (118) | −6.66 | – |
| Controlled displacement location | Mid-span | – |
| Controlled displacement increment | 0.1 | mm |
| Number of solid elements for the concrete bulk | 360\|504 | – |
| Number of beam-bar elements for the reinforcement | 60\|84 | – |



**Fig. 6.** Uni-axial stress-strain relationship of the beam's concrete material.
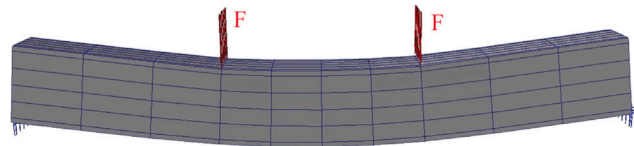


**Fig. 7.** Deformed shape of the beam.

The stress–strain diagram of the concrete material used in the beam analysis is depicted in Fig. 6, which is obtained under uni-axial stress conditions. Although concrete's tensile capacity is not expected to have any significant influence on the structural behaviour, alternatively we have used a single surface concrete material model by removing the Rankine cut-off surface in the plastic return process, whose uniaxial test is also shown in Fig. 6.

*6.1.1. Results of the beam analysis*

The developed model is compared against two other numerical models presented in [41] as MAFEM, Precon3D, as well as experimental results presented in [58]. The model MAFEM, is based on Modified Mohr–Coulomb yield surface capturing the compression and Rankine yield surface capturing the tensile regime of the concrete material. Thus, the compared MAFEM numerical model is also based on a multi-surface plasticity approach and implemented within a 3D solid element-based software, making it particularly relevant for our analysis. Secondly, Precon3D results also reported in [41] were used for comparisons with the currently developed tool. Precon3D can also simulate the three-dimensional concrete material behaviour. Thirdly, the experimental results reported in [58] were used for the purpose of validating our model's accuracy in predicting the behaviour of real reinforced concrete beams. We present the deformed shape of the beam element in Fig. 7, which is obtained by using an amplification factor for the deflections to provide a graphical confirmation of the expected behaviour.

The load–deflection curves are depicted in Fig. 8, which shows that the developed model demonstrates a high level of accuracy in capturing the initial stiffness of the material, closely mirroring the nonlinear response observed in the experimental study as well as in the numerical studies in [41,58]. Fig. 8 also shows that mesh refinement did not have significant effect on the results and thus, the adopted meshes can be deemed sufficient. The level of precision in the results confirms that the developed model is accurate in simulating the behaviour of the reinforced concrete beam subjected to the four-point bending test. In Fig. 8, we have also shown the results of the single surface model based on the 360 solid-element mesh. It can be verified that the increased tensile strength of the single-surface model shown in the material test in Fig. 6 has very little influence on the results.
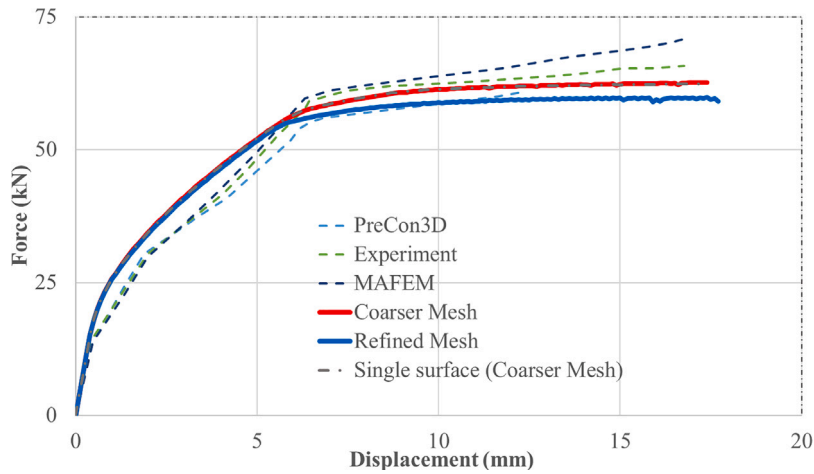
**Fig. 8.** Force - mid-span displacement diagram of the beam.

**Table 3**
Material properties of the reinforced concrete column.

| Material | Properties | Values | Unit |
|---|---|---|---|
| Concrete | Young modulus, $E_c$ | 25 000 | MPa |
| | Poisson ratio, $\nu$ | 0.18 | – |
| | Compression strength, $\sigma_c$ | 30.61 | MPa |
| | Tensile strength, $\sigma_t$ | 3.15 | MPa |
| | Strain at compression peak | 0.0027 | – |
| | Strain at tensile peak | 0.0002 | – |
| Steel | Young modulus, $E_s$ | 210 000 | MPa |
| | Yield strength (longitudinal), $\sigma_y$ | 490 | MPa |
| | Yield strength (stirrups), $\sigma_y$ | 206 | MPa |
| | Diameter of the longitudinal rebars | 25 | mm |
| | Diameter of the stirrups | 12 | mm |

**Table 4**
Parameters of the software for the column analysis.

| Parameters | Values | Units |
|---|---|---|
| Onset ratio plastic flow $k_o$ in Eq. (112) | 0.03 | – |
| Slope linear potential surface $B$ in Eq. (118) | −10.00 | – |
| Controlled displacement location | Mid-span | – |
| Controlled displacement increment | 0.1 | mm |
| Number of solid elements for the concrete bulk | 288\|544 | – |
| Number of beam-bar elements for the reinforcement | 216\|288 | – |

## 6.2. Eccentrically loaded column test

The second case study is the analysis of an eccentrically loaded reinforced column that was also investigated both experimentally and numerically in [59]. The column is simply supported as shown in Fig. 9, which has a square cross-section of 300 mm by 300 mm and a height of 2000 mm. It was reinforced with longitudinal bars and transverse stirrups. The compressive force was applied to the concrete column at both ends with an eccentricity of 60 mm. By introducing the eccentric loading, the experimental set up aims to induce bending moments alongside compressive internal forces, providing a combined case. The detail of the column's reinforcements is depicted in Fig. 9. The material properties of the column are provided in Table 3. The numerical model developed for the column case study is constructed first by using a $4 \times 4$ element-mesh over the cross-section and 18-element mesh along the span resulting with 288 solid elements for the concrete bulk. Considering the 50 mm cover on both sides, there are $4 \times 16 = 64$ beam elements used for the longitudinal rebars and 152 beam elements used for the stirrups. Alternatively, we have used a refined mesh by further dividing the column span into 34 elements, resulting with a 544 solid-element mesh for the concrete bulk. Accordingly, in the refined mesh, 128 beam elements used for the longitudinal bars and 288 beam elements were used for the stirrups. The configuration of longitudinal bars and stirrups within the model is carefully aligned with the column's set up, as detailed in Fig. 9, ensuring that the numerical model replicates the physical experiment. The key analysis parameters are provided in Table 4.
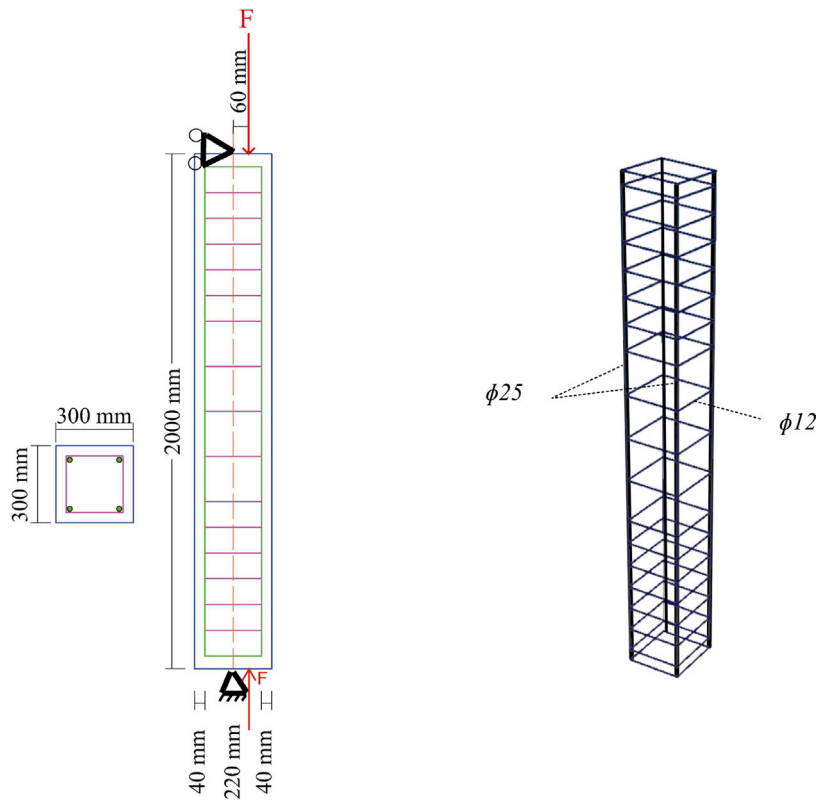
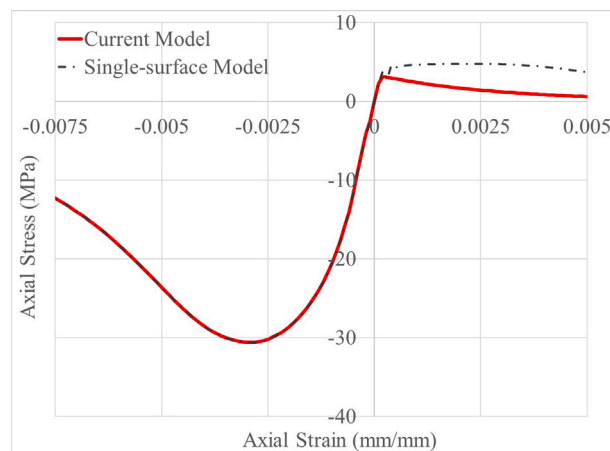**Fig. 9.** Geometry, boundary conditions and loading of the column.



**Fig. 10.** Uni-axial stress-strain relationship of the column's concrete material.

The stress–strain diagram of the concrete material used in the column analysis is depicted in Fig. 10, which is obtained under uni-axial stress conditions. Alternatively, we have used a single surface concrete material model by removing the Rankine cut-off surface in the plastic return process, whose uniaxial test is also shown in Fig. 10.

### 6.2.1. Results of the column analysis

The deformed shape of the finite element model of the RC column is presented in Fig. 11, which has been magnified by using an amplification factor. The figure confirms that the bending behaviour is significant, which is a direct consequence of the applied eccentric load. The asymmetry in the deflection profile is particularly noteworthy, as it suggests the influence of the eccentric load in generating a non-uniform distribution of internal stresses and strains within the column. In examining the column's response, we
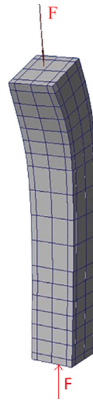
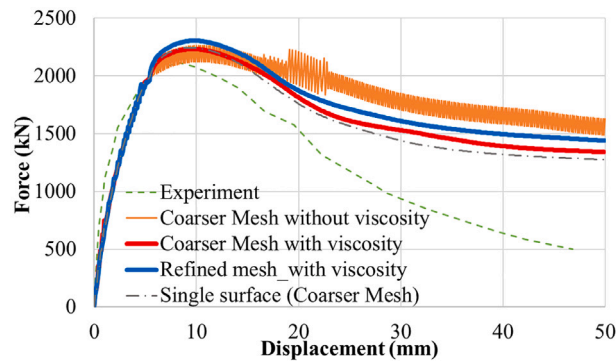**Fig. 11.** Deformed shape of the column.



**Fig. 12.** Force - mid-span displacement diagram of the column.

have produced the force-midspan displacement diagram in Fig. 12, which provides a comparison between the experimental data and the current numerical model. The experimental curve indicates a linearly elastic behaviour up to approximately 100 kN, followed by a nonlinear response leading to a peak force near 2100 kN, before a gradual decrease in force indicating the progressive failure of the column. The current model shows a similar initial linear trend, indicating an accurate representation of the details of the column. However, the model predicts a slightly higher peak force, reaching this maximum at a smaller displacement in the model compared to the experiment. Overall, the graphs align closely in terms of general characteristics of the column's behaviour. It can also be seen from Fig. 12 that the difference between the results of two alternative meshes are not significant. It should be noted that the results without the viscous regularization depicts significant oscillatory behaviour beyond the peak strength. On the other hand, viscous regularization completely suppresses the oscillations and for both meshes we have obtained smooth curves as shown in Fig. 12. In Eqs. (99) and (100), we have used $\psi \Delta t = 1$ which was decided after numerical experimentation. It should be noted that overly large values can create significant damping influence and artificially increase the observed strength. Therefore, we have tried to pick a $\psi \Delta$ that is large enough to suppress the oscillations and small enough not to influence the strength. As also presented in Fig. 12 the difference between the results based on multi-surface and single surface plasticity assumptions are not significant.

### 6.3. Laterally loaded shear-wall test

In the third case study, we apply cyclic load on a reinforced concrete slender shear-wall tested in [60] under cyclic load. The analysed shear-wall has 1750 mm height, 700 mm width, and 100 mm thickness. The concrete cover is maintained at 10 mm. The load application point is situated 1750 mm above the base, aligning with the experimental set up. A constant axial load of G = 287 kN is applied at the top of the shear-wall as shown in Fig. 13. The arrangement of longitudinal bars and stirrups within the model precisely matches the configuration of the shear-wall, to make sure that the numerical analysis closely reflects the experimental test. The reinforcement layout includes four Ø10 mm longitudinal bars at the wall's boundaries and six Ø8 mm bars arranged in two layers for vertical web reinforcement, supplemented by Ø5 mm bars spaced at 90 mm intervals for horizontal reinforcement. The vertical reinforcement bars, classified as A630-420H, have a yield strength of 420 MPa, whereas the horizontal bars, identified as AT560-500H, boast a yield strength of 500 MPa. The concrete utilized has a confirmed mean strength of 27.4 MPa. To capture the change in the stiffness during unloading, we have included the damage component of the material. We have used isotropic only damage for its ease of calibration while comparing our results with those of the experiment. The stress–strain diagram of the concrete material
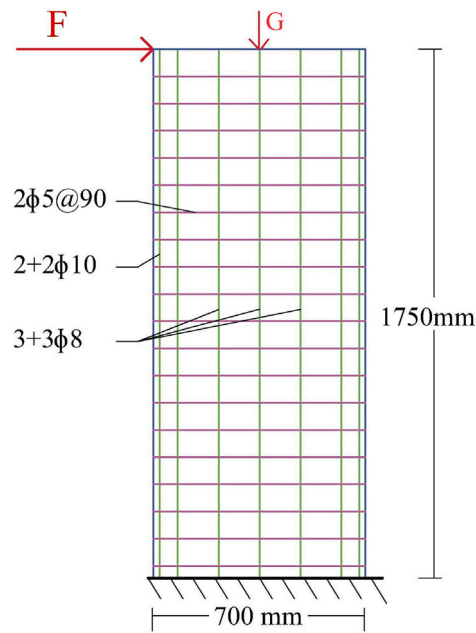
**Fig. 13.** Geometry, boundary conditions and loading of the shear-wall.

**Table 5**
Material properties of the reinforced concrete shear-wall.

| Material | Properties | Values | Unit |
|---|---|---|---|
| Concrete | Young modulus, $E_c$ | 32 700 | MPa |
| | Poisson ratio, $\nu$ | 0.15 | – |
| | ConcreteCompressiveStress, | 27.4 | MPa |
| | Tensile strength, $\sigma_t$ | 3.0 | MPa |
| | Strain at compression peak | 0.00275 | – |
| | Strain at tensile peak | 0.0001 | – |
| Steel Ø5 | Young modulus, $E_s$ | 225 000 | MPa |
| | Yield strength, $\sigma_y$ | 608.9 | MPa |
| Steel Ø8 | Young modulus, $E_s$ | 225 000 | MPa |
| | Yield strength, $\sigma_y$ | 445.6 | MPa |
| Steel Ø10 | Young modulus, $E_s$ | 224 000 | MPa |
| | Yield strength, $\sigma_y$ | 469.2 | MPa |

used in the shear-wall analysis is depicted in Fig. 14, which is obtained under uni-axial stress conditions. Additional properties for the material modelling are provided in Table 5. Two alternative meshes were considered for the finite element modelling of the shear-wall. The first model was built with 672 solid elements and 630 beam elements by dividing the cross-section into $4 \times 8 = 32$ mesh and using 21 elements along the height. In the second more refined mesh we have used 32 elements along the height which resulted with 1024 solid elements and 784 beam elements for the total reinforcement. The essential solution parameters guiding the numerical investigation, are provided in Table 6.

### 6.3.1. Results of the shear-wall analysis

The exaggerated deformed shape of the finite element model of the reinforced concrete shear-wall is depicted in Fig. 15. From the examination of the cyclic force - displacement diagram in Fig. 16, it can be confirmed that the damage component of the material model causes stiffness reduction within each cycle. The predicted behaviour of the shear-walls by the developed model can be seen to generally agree well with the experimental results presented in [60]. It can be observed from Fig. 16 that the differences caused by the single surface assumption and mesh refinement accumulate under cyclic loading and therefore, the differences are more noticeable towards the later cycles.

**Table 6**

Parameters of the software for the shear-wall analysis.

| Parameters | Values | Units |
|---|---|---|
| Onset ratio plastic flow $k_o$ in Eq. (112) | 0.2 | – |
| Slope linear potential surface $B$ in Eq. (118) | −12.5 | – |
| Damage coefficient for compression $C$ in Eq. (121) | 0.36 | – |
| Damage coefficient for tension $C$ in Eq. (121) | 0.16 | – |
| Controlled displacement location | Tip | – |
| Controlled displacement increment | 0.25 | mm |
| Number of cycles | 21 | – |
| Number of solid elements for the concrete bulk | 672\|1024 | – |
| Number of beam-bar elements for the reinforcement | 630\|784 | – |
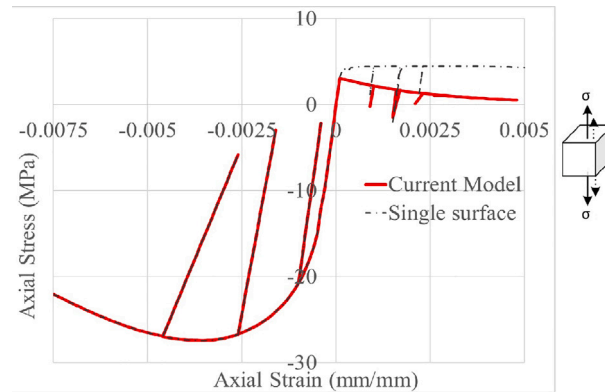


**Fig. 14.** Uni-axial cyclic stress-strain relationship of the wall's concrete material.
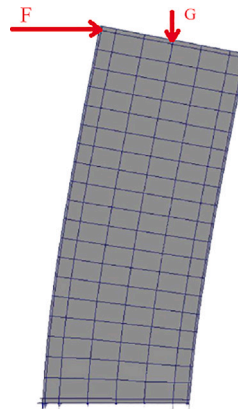


**Fig. 15.** Deformed shape of the shear-wall.

### 6.4. Cyclic column compression test

In our final case study, we have modelled a concentrically loaded reinforced column under cyclic loading to illustrate the effect of anisotropic damage assumption. We have used the 1000 mm high, square column of 300 mm by 300 mm cross-section. We have used Ø25 steel for the longitudinal rebars as well as the stirrups as shown in Fig. 17, whose properties are given in Table 7. However, to illustrate the effect of anisotropic damage, we have also removed the confinement. The material properties of the column are provided in Table 7. The numerical model developed for the column case study is constructed by using 275 solid elements and 84 beam elements for the longitudinal rebars, and when exist 88 beam elements for the stirrups. The key analysis parameters are provided in Table 8.

We have used three alternative assumptions for the damage behaviour, namely; isotropic-only, anisotropic-only and anisotropic, corresponding to $C$ values of 0.36\|0\|0.25 and $\omega$ values of 0\|$10 \times 10^4$\|$5 \times 10^4$ as given in Table 8, respectively. The last case referred to as anisotropic is the combination of isotropic and anisotropic components calibrated by using $C = 0.25$ and $\omega = 5 \times 10^4$. As shown in
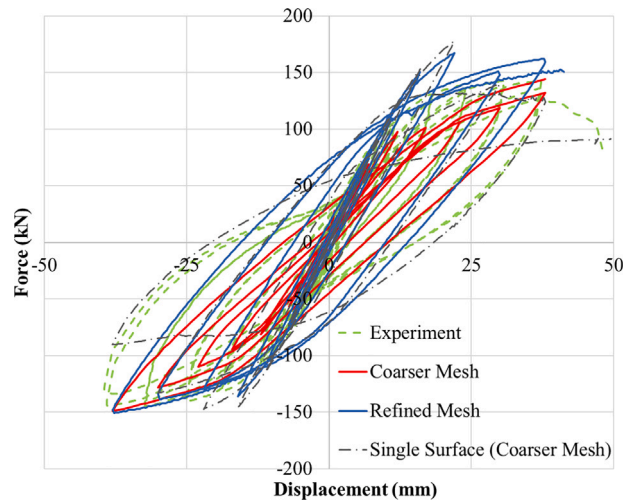
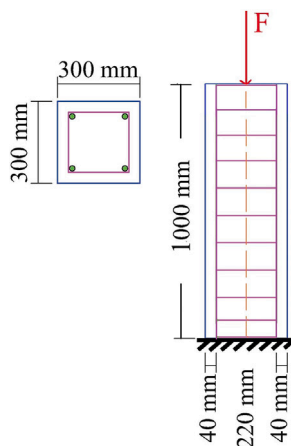**Fig. 16.** Force - tip displacement diagram of the shear-wall.



**Fig. 17.** Geometry, boundary conditions and loading of the column.

**Table 7**

Material properties of the reinforced concrete column.

| Material | Properties | Values | Unit |
|---|---|---|---|
| Concrete | Young modulus, $E_c$ | 32 700 | MPa |
| | Poisson ratio, $v$ | 0.15 | – |
| | ConcreteCompressiveStress, | 27.4 | MPa |
| | Tensile strength, $\sigma_t$ | 3.0 | MPa |
| | Strain at compression peak | 0.00275 | – |
| Steel Ø25 | Young modulus, $E_s$ | 210 000 | MPa |
| | Yield strength, $\sigma_y$ | 490 | MPa |

Fig. 18, all three material models were intended to have almost identical behaviour under uni-axial stress–strain test and calibrated accordingly.

### 6.4.1. Results of the cyclic column analysis

The deformed shape of the finite element model of the RC column is presented in Fig. 19, which has been magnified by using an amplification factor. The figure confirms that the loading is only axial. In examining the column's response, we have produced the force-midspan displacement diagram in Fig. 20 for both confined and unconfined models. It can be verified from Fig. 20 that during unloading the slopes of the confined model differ more significantly between isotropic-only, anisotropic-only and (combined) anisotropic damage assumptions, which approximately correspond to, $2.6 \times 10^3$ kN/mm, $1.5 \times 10^3$ kN/mm and

**Table 8**

Parameters of the software for the column analysis.

| Parameters | Values | Units |
|---|---|---|
| Onset ratio plastic flow $k_o$ in Eq. (112) | 0.2 | – |
| Slope linear potential surface $B$ in Eq. (118) | −12.5 | – |
| Isotropic damage coefficient $C$ in Eq. (121) | 0.36\|0\|0.25 | – |
| Anisotropic damage coefficient $\omega$ in Eq. (32) | 0\|10 × 10⁴\|5 × 10⁴ | – |
| Controlled displacement location | Tip | – |
| Controlled displacement increment | 0.05 | mm |
| Number of cycles | 3 | – |
| Number of solid elements for the concrete bulk | 160 | – |
| Number of elements for the axial reinforcement | 40 | – |
| Number of beam elements for the stirrups | 88 | – |
| Number of beam elements for the ties | 22 | – |
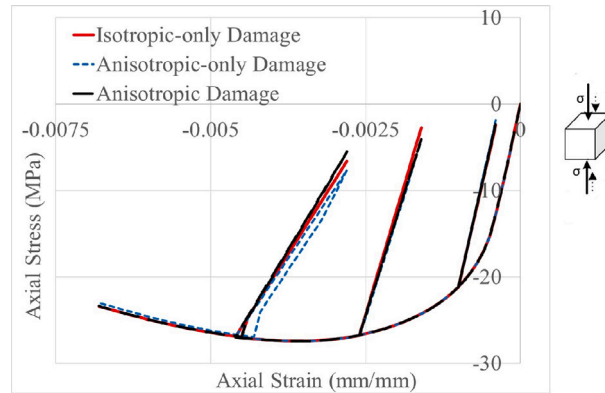


**Fig. 18.** Uni-axial stress-strain relationship of the column's concrete material.
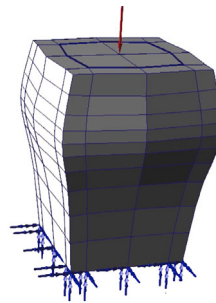


**Fig. 19.** Deformed shape of the column.

$2.2 \times 10^3$ kN/mm, respectively. For the unconfined test the slopes of the isotropic-only, anisotropic-only and (combined) anisotropic damage assumptions, can be calculated from Fig. 20 as $1.82 \times 10^3$ kN/mm, $1.6 \times 10^3$ kN/mm and $1.7 \times 10^3$ kN/mm, respectively. From the identified numbers, it can be verified that between isotropic only and anisotropic only assumptions the ratio of the slopes is $2.6/1.5 = 1.72$ is for the confined column, whereas the same comparison provides the ratio of $1.82/1.6 = 1.14$ for the unconfined column. As the calibrations were made based on the uni-axial material test it is expected for different damage assumptions to agree for the unconfined case. It is however, interesting to note that when confinement is increased the predictions of different damage assumptions start to differ more significantly.

## 7. Conclusions

We have developed a novel Elastic-Plastic-Anisotropic-Damage material model where the evolution of both the isotropic and anisotropic components of the damage are completely based on accumulated plastic strains. In the case of plastic evolution during loading, the procedure assures complete independence of the plastic return operations from the damage update. On the other hand, in the case of elastic unloading, the damage component of the strain can be obtained directly from the total strain and a matrix of damage evolution. We have adopted the novel Elastic-Plastic-Anisotropic-Damage material to model the three-dimensional behaviour
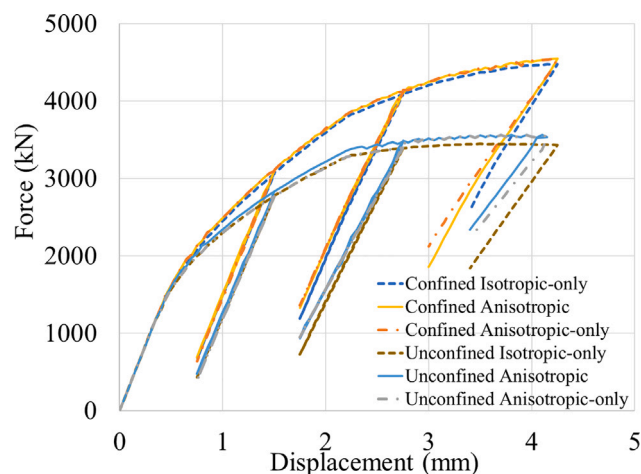
**Fig. 20.** Force - tip axial displacement diagram of the column.

of the concrete material. For this purpose, we have used multi-surface non-associative plasticity. The pressure-sensitive concrete material model is based on the Menetrey–Willam criterion for the dominant compression stresses and the Rankine criterion for dominant tension stresses. Effects of the loading history can be reflected by the hardening/softening and damage variables of the model, which are conveniently updated after convergence. Calibration parameters of the material model conveniently depend only on the uni-axial stress–strain relationship. As a result, the concrete material behaviour is determined by the elementary material parameters i.e., Elasticity modulus, Poisson's ratio, maximal uni-axial tensile and compression stresses and the plastic stress limit. A simple linear potential function was adopted which depends only on one calibration parameter. We have identified that the linear potential surface provides efficiency in terms of the computational procedure as the Hessian matrix vanishes and tangent modulus is easier to calculate. The developed concrete material model was successfully integrated in the developed in-house fortran finite element software and was applied for the analysis of a reinforced beam, column and shear-wall. Monotonic as well as cyclic loading cases were included in the case studies. The results based on the developed methodology has generally provided very good agreement with physical experiments as well as numerical results from the literature. The case studies have shown that the ultimate strength and deformation capacity of various structural components can be captured, which verifies the suitability of the developed tool for the capacity analysis of reinforced concrete structures under various conditions. We have also demonstrated the method's numerical performance by running mesh refinement tests on the case studies. Furthermore, we have introduced a viscous regularization strategy to provide numerical stability when oscillatory behaviour is observed due to material softening. The effect of anisotropic damage assumption as opposed to isotropic only damage assumption was also illustrated on a column cyclic test, which was shown to have influence on the slopes of the load deflection curves during unloading depending on the confinement of the column.

## CRediT authorship contribution statement

**A. Torabizadeh:** Writing – review & editing, Visualization, Validation, Investigation. **A. Sarikaya:** Writing – review & editing, Writing – original draft, Validation, Methodology. **R.E. Erkmen:** Writing – review & editing, Writing – original draft, Visualization, Validation, Supervision, Software, Methodology, Investigation, Conceptualization.

## Declaration of competing interest

The authors declare that they have no known competing financial interests or personal relationships that could have appeared to influence the work reported in this paper.

## Acknowledgements

## References

[1] N.S. Ottosen, A failure criterion for concrete, J. Eng. Mech. Div. 103 (4) (1977) 527–535.
[2] D. Han, W.-F. Chen, Constitutive modeling in analysis of concrete structures, J. Eng. Mech. 113 (4) (1987) 577–593.
[3] W. Chen, Concrete plasticity: Macro-and microapproaches, Int. J. Mech. Sci. 35 (12) (1993) 1097–1109.
[4] P. Menetrey, K. Willam, Triaxial failure criterion for concrete and its generalization, Struct. J. 92 (3) (1995) 311–318.
[5] H.D. Kang, K.J. Willam, Localization characteristics of triaxial concrete model, J. Eng. Mech. 125 (8) (1999) 941–950.

[6] P. Grassl, K. Lundgren, K. Gylltoft, Concrete in compression: a plasticity theory with a novel hardening law, Int. J. Solids Struct. 39 (20) (2002) 5205–5223.
[7] P. Grassl, Modelling of dilation of concrete and its effect in triaxial compression, Finite Elem. Anal. Des. 40 (9–10) (2004) 1021–1033.
[8] J. Bao, X. Long, K.H. Tan, C.K. Lee, A new generalized Drucker–Prager flow rule for concrete under compression, Eng. Struct. 56 (2013) 2076–2082.
[9] M. Klisiński, Z. Mroz, Description of inelastic deformation and degradation of concrete, Int. J. Solids Struct. 24 (4) (1988) 391–416.
[10] G. Meschke, R. Lackner, H.A. Mang, An anisotropic elastoplastic-damage model for plain concrete, Int. J. Numer. Methods Eng. 42 (4) (1998) 703–727.
[11] J. Lee, G.L. Fenves, Plastic-damage model for cyclic loading of concrete structures, J. Eng. Mech. 124 (8) (1998) 892–900.
[12] R.K.A. Al-Rub, G.Z. Voyiadjis, On the coupling of anisotropic damage and plasticity models for ductile materials, Int. J. Solids Struct. 40 (11) (2003) 2611–2643.
[13] M. Brünig, An anisotropic ductile damage model based on irreversible thermodynamics, Int. J. Plast. 19 (10) (2003) 1679–1713.
[14] M. Brünig, A. Michalski, A stress-state-dependent continuum damage model for concrete based on irreversible thermodynamics, Int. J. Plast. 90 (2017) 31–43.
[15] J. Lubliner, J. Oliver, S. Oller, E. Onate, A plastic-damage model for concrete, Int. J. Solids Struct. 25 (3) (1989) 299–326.
[16] I. Doghri, Numerical implementation and analysis of a class of metal plasticity models coupled with ductile damage, Internat. J. Numer. Methods Engrg. 38 (20) (1995) 3403–3431.
[17] P. Grassl, M. Jirásek, Damage-plastic model for concrete failure, Int. J. Solids Struct. 43 (22–23) (2006) 7166–7196.
[18] G.Z. Voyiadjis, Z.N. Taqieddin, P.I. Kattan, Anisotropic damage–plasticity model for concrete, Int. J. Plast. 24 (10) (2008) 1946–1965.
[19] F. Armero, S. Oller, A general framework for continuum damage models. I. Infinitesimal plastic damage models in stress space, Int. J. Solids Struct. 37 (48–50) (2000) 7409–7436.
[20] A. Ibrahimbegovic, Nonlinear Solid Mechanics: Theoretical Formulations and Finite Element Solution Methods, vol. 160, Springer Science & Business Media, 2009.
[21] B. Ayhan, P. Jehel, D. Brancherie, A. Ibrahimbegovic, Coupled damage–plasticity model for cyclic loading: Theoretical formulation and numerical implementation, Eng. Struct. 50 (2013) 30–42.
[22] A. Ibrahimbegovic, P. Jehel, L. Davenne, Coupled damage-plasticity constitutive model and direct stress interpolation, Comput. Mech. 42 (1) (2008) 1–11.
[23] A. Sarikaya, R. Erkmen, A plastic-damage model for concrete under compression, Int. J. Mech. Sci. 150 (2019) 584–593.
[24] S. Murakami, N. Ohno, A continuum theory of creep and creep damage, in: Creep in Structures: 3rd Symposium, Leicester, UK, September 8–12, 1980, Springer, 1981, pp. 422–444.
[25] S. Murakami, Notion of continuum damage mechanics and its application to anisotropic creep damage theory, 1983.
[26] C. Chow, J. Wang, An anisotropic theory of continuum damage mechanics for ductile fracture, Eng. Fract. Mech. 27 (5) (1987) 547–558.
[27] V.A. Lubarda, D. Krajcinovic, Damage tensors and the crack density distribution, Int. J. Solids Struct. 30 (20) (1993) 2859–2877.
[28] G.Z. Voyiadjis, B. Deliktas, A coupled anisotropic damage model for the inelastic response of composite materials, Comput. Methods Appl. Mech. Engrg. 183 (3–4) (2000) 159–199.
[29] J.-L. Chaboche, Continuous damage mechanics—a tool to describe phenomena before crack initiation, Nucl. Eng. Des. 64 (2) (1981) 233–247.
[30] M.L. Kachanov, A microcrack model of rock inelasticity part I: Frictional sliding on microcracks, Mech. Mater. 1 (1) (1982) 19–27.
[31] J. Cordebois, F. Sidoroff, Endommagement anisotrope en élasticité et plasticité, 1982.
[32] C. Chow, J. Wang, A finite element analysis of continuum damage mechanics for ductile fracture, Int. J. Fract. 38 (1988) 83–102.
[33] S. Murakami, Mechanical modeling of material damage, 1988.
[34] J. Lemaitre, R. Desmorat, M. Sauzay, Anisotropic damage law of evolution, Eur. J. Mech. A Solids 19 (2) (2000) 187–208.
[35] M. Jirasek, Z.P. Bazant, Inelastic Analysis of Structures, John Wiley & Sons, 2001.
[36] R. Wan, Implicit integration algorithm for Hoek-Brown elastic-plastic model, Comput. Geotech. 14 (3) (1992) 149–177.
[37] P. Fuschi, M. Dutko, D. Perić, D. Owen, On numerical integration of the five-parameter model for concrete, Comput. Struct. 53 (4) (1994) 825–838.
[38] V.K. Papanikolaou, A.J. Kappos, Confinement-sensitive plasticity constitutive model for concrete in triaxial compression, Int. J. Solids Struct. 44 (21) (2007) 7021–7048.
[39] T. Yu, J. Teng, Y. Wong, S. Dong, Finite element modeling of confined concrete-II: Plastic-damage model, Eng. Struct. 32 (3) (2010) 680–691.
[40] J. Červenka, V.K. Papanikolaou, Three dimensional combined fracture–plastic material model for concrete, Int. J. Plast. 24 (12) (2008) 2192–2220.
[41] M. Galic, P. Marovic, Z. Nikolic, Modified Mohr-Coulomb–Rankine material model for concrete, Eng. Comput. 28 (7) (2011) 853–887.
[42] D. Lu, X. Du, G. Wang, A. Zhou, A. Li, A three-dimensional elastoplastic constitutive model for concrete, Comput. Struct. 163 (2016) 41–55.
[43] E. Pramono, K. Willam, Implicit integration of composite yield surfaces with corners, Eng. Comput. 6 (3) (1989) 186–197.
[44] G. Hofstetter, J.C. Simo, R.L. Taylor, A modified cap model: closest point solution algorithms, Comput. Struct. 46 (2) (1993) 203–214.
[45] P.H. Feenstra, R. De Borst, A composite plasticity model for concrete, Int. J. Solids Struct. 33 (5) (1996) 707–730.
[46] S. Dolarevic, A. Ibrahimbegovic, A modified three-surface elasto-plastic cap model and its numerical implementation, Comput. Struct. 85 (7–8) (2007) 419–430.
[47] D.P. Adhikary, C.T. Jayasundara, R.K. Podgorney, A.H. Wilkins, A robust return-map algorithm for general multisurface plasticity, Internat. J. Numer. Methods Engrg. 109 (2) (2017) 218–234.
[48] S. Pech, M. Lukacevic, J. Füssl, A robust multisurface return-mapping algorithm and its implementation in Abaqus, Finite Elem. Anal. Des. 190 (2021) 103531.
[49] W.T. Koiter, Stress-strain relations, uniqueness and variational theorems for elastic-plastic materials with a singular yield surface, Q. Appl. Math. 11 (3) (1953) 350–354.
[50] J.C. Simo, J. Ju, Strain-and stress-based continuum damage models—I. Formulation, Int. J. Solids Struct. 23 (7) (1987) 821–840.
[51] J.C. Simo, T.J. Hughes, Computational Inelasticity, vol. 7, Springer Science & Business Media, 2006.
[52] W. Zhang, Y. Cai, Continuum Damage Mechanics and Numerical Applications, Springer Science & Business Media, 2010.
[53] G. Monti, C. Nuti, Nonlinear cyclic behavior of reinforcing bars including buckling, J. Struct. Eng. 118 (12) (1992) 3268–3284.
[54] X. Liu, S. Yan, K.J. Rasmussen, G.G. Deierlein, Verification of void growth-based exponential damage function for ductile crack initiation over the full range of stress triaxialities, Eng. Fract. Mech. 269 (2022) 108571.
[55] R.D. Cook, et al., Concepts and Applications of Finite Element Analysis, John wiley & sons, 2007.
[56] J.-L. Batoz, G. Dhatt, Incremental displacement algorithms for nonlinear problems, Internat. J. Numer. Methods Engrg. 14 (8) (1979) 1262–1267.
[57] A. Ibrahimbegovic, E.L. Wilson, Thick shell and solid finite elements with independent rotation fields, Int. J. Numer. Methods Eng. 31 (7) (1991) 1393–1414.
[58] S. Majewski, R. Krzywon, Numerical and experimental verification of FEM for elastoplastic analysis of RC structures and soil structure interaction problems, in: Proceedings of the 7th International Conference on Numerical Methods in Continuum Mechanics, High Tatras, October, University of Zilina, Zilina, 1998, pp. 519–524.
[59] J. Němeček, Z. Bittnar, Experimental investigation and numerical simulation of post-peak behavior and size effect of reinforced concrete columns, Mater. Struct. 37 (2004) 161–169.
[60] M. Hube, A. Marihuén, J.C. de la Llera, B. Stojadinovic, Seismic behavior of slender reinforced concrete walls, Eng. Struct. 80 (2014) 377–388.